Author‘s response to two anonymous reviews for ACP-2020-584

We thank the two anonymous referees for their constructive feedback, which significantly improved the quality of the manuscript. We are well aware of how much work such a report requires. Due to the extensive modifications of the manuscript, we compose a combined author’s response for both reviews. First, we summarize general revisions of the manuscript. Second, we refer to the remarks of each reviewer individually. The original reviewer comments are marked in blue color.

General remarks

- The structure of the manuscript has been completely revised.
- A new section about technical aspects of humidity measurements under cold and cloudy conditions has been implemented. We want to make sure that the observed humidity inversions are real and not a measurement artifact. The main reason for this was the observation of systematic humidity differences when comparing ascents and subsequent descents. We discuss error sources for the RH measurements and improve the measurements with a revised time-response correction based on further laboratory investigations.
- Due to the improved correction of humidity observations, data observed during descents are now more consistent and therefore included in the data analysis. For the descents we observed an interesting phenomenon: During all flights, the cloud base descended between ascent and descent, but in a different way. This behavior was confirmed by remote sensing. Due to the increased number of profiles with different relative locations of temperature inversion, SHI and cloud top, further scientific questions could be analyzed.
- We revised the analysis of turbulent fluxes, see specific comments below.
- We tried to focus on the novelty of our measurements rather than on uncertainties, as suggested by reviewer #1.
- Both reviewers criticize that it is hard to generalize from case studies. In our study, we document and analyze the observed cases and agree that the results should not be generalized. Further observations over a larger measurement period are needed for a more general conclusion, as stated in our summary.
- Reviewer # 1 suggested shifting the LES to a separate paper, reviewer # 2 appreciated the combination of observations and LES. We decided on a compromise and now discuss one LES case to show the impact of the SHI on the cloud, leaving potential for a more detailed separate study. See also the answer to the specific comment of reviewer # 1 below.

Remarks to comments of referee # 1

- Excessively long and tedious title.

  We agree and change the title to “Case study of a humidity layer above Arctic stratocumulus and potential turbulent coupling with the cloud top”.

- Coherent narrative instead of chronological description

  We completely restructured the manuscript. We are confident that this revised version is much more narrative.

- There is no clear hypothesis to test.

  We agree with this point and in the revised version, the main scientific question is raised in the introduction. We don’t word it as a hypothesis, but we think this is a question of style.

- The text even starts with questioning the very existence of moisture inversions, which is off course fine! However, RH for the descending branch from BELUGA is not consistent with the suggested cloud outline; in the upper 50% of the cloud layer, RH < 80%.

  We completely agree with this point, the interpretation of this profile was misleading and not convincing. In the case shown in the first version of the manuscript (old Fig. 1), the cloud extent is estimated from Cloudnet data only for the ascent. For the revised version, we use radar reflectivity raw data with a much higher temporal resolution of 3 s (30 m in vertical) (see new Fig. 2). Here it becomes clear that the balloon descended into a much lower cloud top which partly explains the low humidity in that region. However, there is a general difference in measured RH around cloud top observed during ascents and descents, which motivated us to look deeper into the data resulting in the additional chapter about humidity measurements and an improved correction algorithm.

  For the new technical section about the humidity measurements, we decided to use a different day (5 June, second profile) with a constant cloud top height to clearly show the efficiency of the new corrections.

- Remote sensing retrieval software is wonderful and multi-sensor retrievals, like Cloudnet, has many useful features. This is, however, only true when used carefully and from an understanding of limitations and applicability. Here the authors are using Cloudnet retrievals like a very black box and it doesn’t help much.

  To a large extent, we agree with the reviewer. As a consequence, we had many discussions with our in-house experts for remote sensing observations about this topic. We agreed on using the original cloud radar data with a 30 m vertical resolution to get the most accurate estimate of cloud top development (new Fig. 1 and 2). We considered also including a comparison of remote sensing turbulence observations with BELUGA in-situ

measurements, but finally, we decided that such an analysis - although very interesting - is a different topic which we will consider in a separate manuscript. Turbulence estimated from remote-sensing is only available for in-cloud regions and we focus on the region between cloud-top and the SHI above so remote-sensing does not help very much in this context.

- So instead they bring in LES, which is perhaps an even larger black box but also doesn't help much; what is needed here is some careful thinking, experience and a new analysis strategy. The LES discussion is quite short, and I don't understand why one case is relegated to an Appendix while the other isn't, and it doesn't help at all. I would suggest to expand the LES study and make it a separate paper; base it on this study, by all means, but do the proper set of simulations to figure out the optimal configuration and then do all the different sensitivity simulations you need to extend and generalize whatever it is you find in the analysis of the observations. There are so many ways an LES can be useful, but the way it is used here is not one of them. Multiple initial and boundary condition combinations can bring a simulation to appear similar to a single case-study profile, but there is only one that is correct and it is not always evident which one; most appear correct for the wrong reasons. There is much else to be said about this but most importantly, you should never use an LES to lend credibility to observations; it should be the other way around!

  We appreciate the suggestion to publish the LES study in a separate paper and will keep this option for a more detailed study on how the additional humidity is processed in the cloud layer. However, here we suggest keeping the LES discussion but shift the focus: We don't use the LES as a validation for the measurements. Instead, we focus on one LES case in order to compare with observations to show how the SHI might influence the cloudy ABL. The second LES case, as shown in the appendix, has been removed to the revised version. The technical details about the LES setup are now shifted to the appendix not to destruct the reader from the main point.

- […] the trajectory calculations looks intriguing, but the discussion doesn't seem to go anywhere; you need to do more to be convincing, or should just drop this line of inquiry.

  We agree and omit the trajectory discussion at this point. It might help to explain the source for the humidity layers but this is not the focus of our paper.

- What might help is to explore alternative analysis methods and/or looking at more sources of concurrent observations. I suggest looking more at the remote sensing data independently. For example, directly explore the Doppler data from the cloud radar. There are methods described in the literature how to estimate some turbulence statistics directly from the radar data (e.g. σ_w and ε). An upside to this is that you can find levels where the data comes from a constant altitude for well understood portion of time; flipsides are the lack of resolution and that only one parameter can be derived. But do look at the native time resolution; not the Cloudnet-filtered data.

To broaden our expertise in remote sensing data analysis, we invited Hannes Griesche as co-author. He analyzes the PASCAL remote sensing observations. We considered including turbulence parameters, such as variance and ε derived from the cloud radar data, which gave some interesting insight into cloud dynamics (see Fig. 1 of this document). However, we realized that in-cloud turbulence does not really help to understand the coupling between the SHI and the cloud-top region due to lacking data above the cloud top. Therefore, we decided not to use this kind of analysis in this manuscript. However, these discussions about using radar data more directly helped a lot in improving the cloud top estimates from radar - see new Fig. 2.

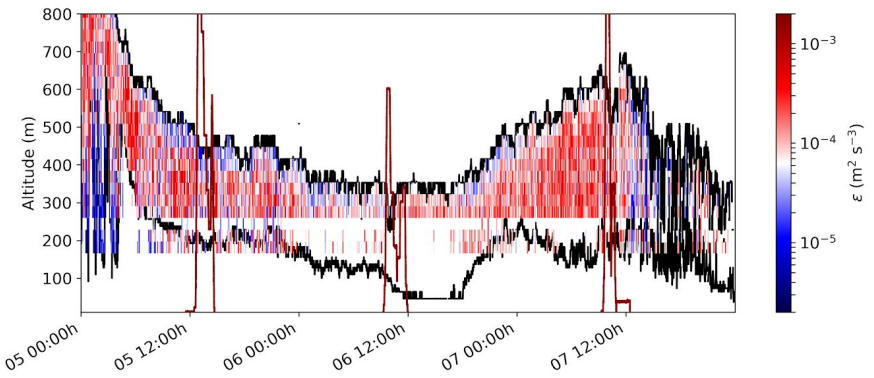

Fig. 1: Eddy dissipation rate estimated from cloud radar data for the observation period.

- Flux discussion:
    - I fail to understand why knowing the size of that flux – from one case – is so important.

      We agree with the concerns about the absolute number of a single flux estimate. The discussion around these numbers and uncertainties was misleading and went in the wrong direction. We now focus more on the general shapes of the vertical profile rather than on absolute magnitudes of fluxes.

    - I would also not walk away from the slant profiles just yet, although they take really careful hands-on analysis. There are several old papers where slant profiles by aircraft have been used to tease out profiles of turbulence statistics with realistic magnitudes and shapes. It does require careful filtering, however, I submit that the vertical velocity of the platform should make aircraft profiles harder to work with than the BELUGA data.

      We stick to the slant profiles, but with slightly changed filter settings. Following arguments by Tjernström (1993) and Lenschow (1988), we set the filter window to 10 s to define the fluctuations from which the local flux is calculated. With this smaller filter window (compared to the ABL-dependent filter window of 50-100 s as applied before), we resolve the smaller structures around the SHI. The flux is then averaged over running 50 s windows on the slant profile.

- However, I would, in contrast, advise against filtering data from constant height flight legs. A numerical filter can never provide a signal with a power spectrum looking anywhere near realistic. So just give it up and use Ogive analysis instead, to analyze the magnitudes of fluxes and variances.

  Ogives are definitely an interesting tool to analyze fluxes. However, as mentioned in previous points, we focus now more on the general vertical structure of the flux profiles instead of estimating fluxes from constant level records.

- A word of warning, however; if the signal looks like in Figure 7a, no filtering in the world will help. The interface between the cloud and the inversion layer is like the surface of a lake and what you see here is the effect of the sensor sometimes being under and sometimes above the "surface". The resulting signal is from two different environments and filtering the signal to make it look smoother will not make those environments the same or even similar; averaging statistics for turbulence over the resulting signal is therefore meaningless, and you need to do something else.

  The reviewer is absolutely right, and we agree that the way the mean fluxes are estimated by filtering records as shown in Fig. 7a is fundamentally wrong. Following the argument that a single value of the flux is not meaningful in this context, we have not included another analysis technique such as Ogive analysis (although we have tried this technique). But we are convinced that a figure like the old Fig. 7 (new Fig. 13) - especially because of the remarkably constant measuring height - can give a valuable impression of the situation around the inversion, and therefore we discuss the observations based on time series. We agree that the reason for a varying z_i is less important here and therefore we will refrain from a corresponding discussion at this place.

- I see no reason to expect the turbulent flux here to be in any other direction than that dictated by the gradient; counter-gradient fluxes appear in deep convective boundary layers, and this is essentially either a near neutral layer close to the upper boundary, in the cloud layer, or a stably stratified environment, in the inversion. So using the flux-gradient approach makes a lot of sense, however, I don't understand the efforts to use parameterizations of the eddy-exchange coefficient, K_q, based on filtered higher-order moments. Why not get it directly from the sensible heat flux and the temperature gradient? If you anyway assume that $K_q = K_H$, this should give you what you want. With the method you use, you can both measure (by eddy-covariance) and calculate (with the flux-gradient method) the sensible heat flux; if the two are different, then you can't trust the parameterized moisture flux either. However, I would say that if the gradient is positive and the flow is turbulent, there's no question in my mind the flux is negative (downward); it just stands to reason, with what we know about turbulent flows. How large it is, is a different question; one that we likely cannot get a useful answer to from one case.

We adopt the reviewer's suggestion and calculate now K_H from the slant profile measurements. We had some internal discussion if it is worth to calculate $K = K(z)$ or to estimate a single K for the region of main interest. With a constant K, we definitively underestimate the flux in the more turbulent cloud layer, but in that region we would have to apply some careful averaging to smooth the local gradients avoiding too much scatter for the K values. We, therefore, decided to estimate K just around the base of the SHI and use this value for the entire profile. These K values differ only slightly among the different days, which gives us some confidence that the method is robust.

- Finally, many are the papers that have tried to explain peculiarities in the results with gravity waves; .... There are, however, methods to show if what you see are indeed buoyancy waves and not just something that happens to look wavy. So – either show up or let up; either you provide some evidence that there are gravity waves present or drop that line of hand-waiving arguments all together.

  We deleted the discussion of possible gravity waves and instead followed the reviewer's argumentation that z_i moves up and down around the instrument, producing those temperature variations. We agree that for our manuscript the exact reason for the variability of z_i is of less importance.

Remarks to comments of referee # 2

- 1) I appreciate the discussion regarding the potential biasing of humidity inversions due to sensor wetting during the ascent through a cloud layer; this has been a caveat or concern in the community for some time, considering many of our climatological frequencies of SHI occurrences have been derived from radiosoundings from field campaigns. It is great to see the ascent/decent profiles of humidity from the BELUGA system do in fact show similar thermodynamic structures to the radio soundings. Have any additional tests been made to attempt to isolate cases where the radiosounding-derived SHIs are potentially biased by sensor wetting, in which case these profiles could be removed from the analysis? I wonder if it would be helpful to broadly estimate the adiabatic liquid water content of the cloud layer from the thermodynamic profiles, and make a comparison with the absolute increase in specific humidity within the SHI (i.e., sensor wetting should likely not exceed the maximum LWC value in the profile). Surely the amount of sensor wetting must be limited by the maximum amount of cloud liquid water content(?).

  We think that the sensor wetting can exceed the maximum LWC in the cloud, as liquid water can accumulate on the sensors. Hence, it is difficult to quantify wet-bulbing, as we don't have an indicator for the extent of wetting. We could not identify wet-bulbing events in the radiosoundings we analyzed. Instead, one case in our BELUGA measurements, where wet-bulbing probably occurred, is the 12 June (see Fig. 2 of this document, not included in the manuscript), where RH increased by almost 10% at cloud top. On this day, we observed wet sensors when they returned to the ground. However, this RH increase causes only a small increase in q as part of the actual SHI.

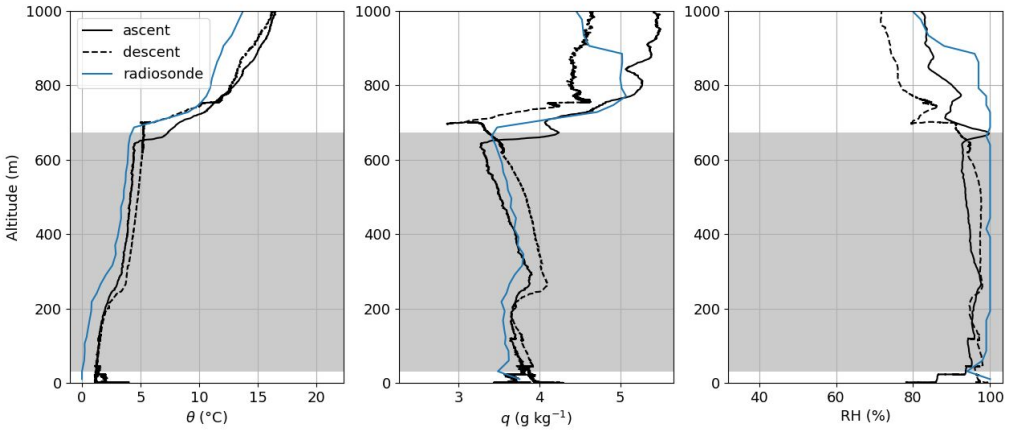

Fig. 2: Vertical profiles for 12 June 2017 (not part of the manuscript).

- 2) The analysis and conclusions derived in this study come from really only 2 profile cases. And even these 2 case have substantial variability in the physical properties of the inversion structures, the flux magnitude estimates, and the turbulence characteristics. I am missing an attempt by the authors to characterize or relate the flux estimates(negative) to the properties of the temperature and humidity inversion layers. How might the displacement depth between SHI base/max and level of largest infrared divergence (cooling) affect the results? I would like to see some more of this substance in the discussion Section 5.

  We address this comment in the new sections 4 and 5 by discussing the descents, where the SHI relates differently to temperature inversion height and cloud top,. However, we cannot relate a flux magnitude to the SHI properties, as we focus on the vertical structure of fluxes rather than a number for cloud-top fluxes.

- Line 26: See/include reference to Devasthale et al. (2011, ACP: “Characteristics of water-vapor inversions observed over the Arctic by Atmospheric Infrared Sounder(AIRS) and radiosondes”)

  Thank you for the reference to this paper about SHIs from radiosondes and satellite data under clear-sky conditions. We inserted the reference in the introduction.

- Line 52. The section heading “Observational” is an adjective, and therefore requires a noun to follow. Please adjust accordingly.

  We changed the heading to “Observations”.

- Line 95. It seems to me, from Fig. 2, that the other two balloon flights during the 5-7th June also correspond with the 12 UTC sounding time and have a continuous ascent and descent profile. The authors should explain, or show, why the results from this soundings and balloon profiles are not shown or described in the text. Do the profile comparisons not look as convincing as in Fig. 1?

We included the new Fig. 2 to show the single flight profiles more in detail and with regard to the cloud. The first flights of 6 and 7 June have constant height steps on the descent. For a comparison between ascent and descent, we now show the second, smaller but continuous profile of 5 June with a constant cloud top height. However, we also included the radiosoundings in the vertical profiles of mean parameters for each day.

- Line 100. It would be helpful to include the cloud boundaries from Cloudnet at the time of the balloon decent as well. This may help to explain the discrepancy between RH and cloud boundaries.

  We now discuss the cloud tops (based on irradiance data) on the ascents and descents for all flights in detail in the new Sect. 4. To discuss the humidity measurements (with a comparison of ascent and descent), we now show another day (5 June) with constant cloud top height.

- Line 114-115: I am confused. I thought the Cloudnet retrievals included ceilometer base heights, MWR liquid water path estimates, and thermodynamic profiles from soundings to retrieve cloud boundaries?

  In the first manuscript version, we showed the cloud base from a separate Ceilometer, which was part of the Polarstern standard meteorological observations. We now use the cloud base data derived from the lidar PollyXT near-field channel, which is part of the Cloudnet sensor suite. The lidar has a resolution of 7.5 m and 30 s. Using native lidar data, not processed with the Cloudnet algorithm, allows detecting cloud base heights below the lowest Cloudnet range gate of 155 m, which is determined by the cloud radar.

- Line 124-125: It would be helpful to include the cloud base and top heights (as colored symbols) on the normalized profiles, in order to show whether (and how deep) the cloud top extended into the temperature and humidity inversion structures.

  We included a separate panel to show the cloud top height (derived from irradiance profiles). We observe almost no cloud tops extending into the inversion.

- Line 145-146: Note additional studies as references: Sedlar et al. (2012, JCLIM);Shupe et al. (2013, ACP); Sedlar and Shupe (2014, ACP); Brooks et al. (2017, JGR).

  We included the suggested references. However, we did not observe that the cloud tops penetrated into the SHIs, as discussed in those studies.

- Line 157: Between which depths in the layer are the Ri number calculated?

  This question is answered by the new columns in Fig. 8-10, showing the vertical profile of the Richardson number.

Case study of a humidity layer above Arctic stratocumulus and potential turbulent coupling with the cloud top

Ulrike Egerer[1], André Ehrlich[2], Matthias Gottschalk[2,a], Hannes Griesche[1], Roel A. J. Neggers[3], Holger Siebert[1], and Manfred Wendisch[2]

[1]Leibniz Institute for Tropospheric Research, Permoserstr. 15, 04318 Leipzig, Germany
[2]Leipzig Institute for Meteorology, University of Leipzig, Stephanstr. 3, 04103 Leipzig, Germany
[3]Institute for Geophysics and Meteorology, University of Cologne, Pohligstr. 3, 50969 Cologne, Germany
[a]Now at Deutscher Wetterdienst, Frankfurter Str. 135, 63067 Offenbach, Germany

Correspondence: Ulrike Egerer (egerer@tropos.de)

Abstract. Specific humidity inversions ~~occur frequently~~ (SHIs) above low-level cloud layers have been frequently observed in the Arctic. The formation of these ~~inversions is often~~ SHIs is usually associated with large scale advection of humid air masses. However, ~~small-scale boundary layer processes interacting with the humidity inversions are~~ the potential coupling of SHIs with cloud layers by turbulent processes is not fully understood~~yet.~~ . In this study, we analyze a three-day period of a persistent layer of increased specific humidity above a stratocumulus cloud observed during an Arctic field campaign in June 2017. The tethered balloon system BELUGA (Balloon-bornE moduLar Utility for profilinG the lower Atmosphere) recorded ~~high-resolution vertical profile measurements of turbulence and radiation~~ vertical profile data of meteorological, turbulence, and radiation parameters in the atmospheric boundary layer. ~~We find that the humidity inversionand the cloud~~ We analyze two different scenarios for the SHI in relation to the cloud top capped by a temperature inversion: (i) the SHI coincides with the cloud top, and (ii) the SHI is vertically separated from the lowered cloud top. In the first case, the SHI and the cloud layer are coupled by ~~eddy dissipation,~~ turbulence extending above the cloud ~~boundary~~ top and linking both layers through turbulent mixing. ~~One case reveals a strong negative virtual sensible heat flux at cloud top(eddy covariance estimate of -15)~~Several profiles reveal downward virtual sensible and latent heat fluxes around cloud top, indicating entrainment of humid air ~~from above into the~~ supplied by the SHI to the cloud layer. For the second case, a downward moisture transport at the base of the SHI and an upward moisture flux at cloud top is observed. Therefore, the area between cloud top and SHI is supplied with moisture from both sides. Finally, Large Eddy Simulations (LES) ~~based on field campaign data are conducted to supplement the flux measurements. Independent experiments for two days confirm the observed entrainment of humid air, reproducing the observed negative~~ complement the observations by modeling a case of the first scenario. The simulations reproduce the observed downward turbulent fluxes of heat and moisture at the cloud top. The LES realizations suggest that in the presence of a ~~humidity layer~~ SHI, the cloud layer remains thicker and the temperature inversion height is ~~slightly raised, reproducing results from previous idealized LES studies. While this acts to prevent cloud collapse, it remains unclear how the additional moisture is processed in the cloud and how exactly it contributes to the longevity of Arctic cloud layers.~~ elevated.

1 Introduction

The Arctic atmospheric boundary layer (ABL) exhibits numerous ~~peculiarities~~ particular features compared to lower latitudes, such as persistent mixed-phase clouds, multiple cloud layers decoupled from the surface~~and ubiquitous vertical~~ , and ubiquitous temperature inversions close to the ~~ground~~surface. Local ABL and cloud processes are complex and not completely understood, but they are considered an important component to explain the rapid warming of the Arctic region (Wendisch et al., 2019). One of the special features frequently observed in the Arctic are specific humidity inversions (SHIs), although specific humidity is generally expected to decrease with height (Nicholls and Leighton, 1986; Wood, 2012). The relative frequency of occurrence of low level SHIs in summer is estimated to be in the range of 70–90 % over the Arctic ocean (Naakka et al., 2018).

Arctic SHIs have been observed during past field campaigns (Sedlar et al., 2012; Pleavin, 2013), e.g., the Surface Heat Budget of the Arctic Ocean (SHEBA; Uttal et al., 2002) in 1997/~~98~~1998, or the Arctic Summer Cloud Ocean Study (ASCOS; Tjernström et al., 2014) in 2008. Furthermore, a number of studies about the climatology of SHIs have been published ~~(e.g. Naakka et al., 2018; Brunke et al., 2015). Over the Arctic ocean,~~ (e.g., Naakka et al., 2018; Brunke et al., 2015; Devasthale et al., 20 . SHIs occur most frequently over the Arctic ocean and are strongest in summer. In the lower troposphere, they often occur in conjunction with temperature inversions and high relative humidity, but ~~they also depend on~~ are also linked to the surface energy budget (Naakka et al., 2018). Formation processes and interactions of SHIs with clouds have been investigated in Large Eddy Simulations (LES). For example, Solomon et al. (2014) showed that a specific humidity layer becomes important as a moisture source for the cloud ~~,~~when moisture supply from the surface is limited. Pleavin (2013) studied how the SHIs support the ~~mixed phase~~ mixed-phase clouds to extend into the temperature and humidity inversion.

Mostly, the formation of the summertime SHIs is attributed to large-scale advection of humid air masses. In the Arctic, especially over sea ice, moisture advection is the critical factor for cloud formation and development (Sotiropoulou et al., 2018). SHIs form when warm, moist continental air is advected over the cold sea ice surface and moisture is removed through condensation and precipitation from the lowest ABL part. This and further simplified formation processes are discussed ~~in~~ by Naakka et al. (2018).

SHIs can contribute to the longevity of Arctic mixed-phase clouds (Morrison et al., 2012; Sedlar and Tjernström, 2009), which ~~influence~~ dominate the near-surface radiation heat budget in the Arctic (Intrieri et al., 2002). When ~~an~~ a SHI is located ~~above a cloud~~closely above an Arctic stratocumulus, it can provide moisture ~~for the cloud~~ that may drive the cloud evolution due to cloud top entrainment. In contrast, in the typical marine sub-tropical or mid-latitude cloud topped ABL, dry air from above is entrained into the cloud (Albrecht et al., 1985; Nicholls and Leighton, 1986; Katzwinkel et al., 2012). Despite their importance for the Arctic near-surface energy budget, SHIs are not well represented in global atmospheric models, where the SHI strength is typically underestimated (Naakka et al., 2018), or the SHIs are not reproduced (Sotiropoulou et al., 2016).

Previous studies ~~about~~ on SHIs are based on radiosoundings, remote sensing observations, reanalysis data, or LES. ~~Local~~ Observational studies based on radiosoundings use profiles of mean thermodynamic parameters and might be influenced by sensor wetting in the SHI region after cloud penetration. Local, small-scale in situ profile observations of SHIs are missing to analyze the exchange processes between the SHI and cloud top. Furthermore, data to characterize and quantify turbulent and

~~radiation properties~~radiative energy fluxes are not available. However, vertical moisture transport close to the cloud top is key to understand the importance of SHIs for the cloud lifetime. ~~Therefore, we perform~~

To investigate the exchange processes between the cloud layer and the SHI, we performed tethered balloon-borne ~~,~~ high-resolution vertical profile measurements of turbulence and radiation ~~recorded within~~ during a three-day period ~~during the~~ in the framework of the Physical Feedbacks of Arctic Boundary Layer, Sea Ice, Cloud and Aerosol (PASCAL) campaign (Wendisch et al., 2019)~~, combined with~~ . The observations are supplemented by LES for the same period. We focus on a detailed case study with a persistent SHI above a stratocumulus deck ~~. Using the observations and simulations, we investigate the local~~ to answer the research question: How are the SHI and the cloud top connected by turbulent mixing?

The paper is structured as follows: Section 2 describes the observations. In Sect. 3, we discuss humidity measurements in cloudy and cold conditions and potential error sources. For the case study, Sect. 4 analyzes the vertical ABL structure around the SHI and ~~study the turbulent transport between~~ the relation of SHI, cloud top, and temperature inversion. In Sect. 5, we investigate the turbulent coupling between SHI and the cloud layer~~.~~ , and the turbulent transport of heat and moisture. We close with a discussion about the impact of the SHI on the cloud by means of LES in Sect. 6.

2 ~~Observational~~

2 Observations

2.1 The PASCAL expedition

The observations analyzed in this study were performed during PASCAL (Wendisch et al., 2019), which took place in the sea-ice covered area north of Svalbard in summer 2017. The RV *Polarstern* (Knust, 2017) carried a suite of remote sensing and in situ instrumentation. Additionally, an ice floe camp was erected in the vicinity of the ship (Macke and Flores, 2018). Knudsen et al. (2018) describe the ~~ice floe period~~ synoptic situation during the operation of the ice floe camp as climatologically warm with prevailing warm and moist maritime air masses advected from the South and East. The meteorological conditions were influenced by a high pressure ridge east of Svalbard. The present study is based on measurements with instruments carried by the tethered balloon system BELUGA (Balloon-bornE moduLar Utility for profilinG the lower Atmosphere; Egerer et al., 2019). BELUGA was launched from the sea ice floe at around 82° N, 10° E in the period of 5–14 June 2017. The balloon measurements are complemented by radiosoundings launched every six hours (Schmithüsen, 2017) and by ship-based remote sensing ~~data from radar and lidar , which are~~ observations from a vertical pointing, motion stabilized cloud radar (Griesche et al., 2020c), a lidar (Griesche et al., 2020b) and a microwave radiometer of the OCEANET platform (Griesche et al., 2020), which were processed with the ~~Cloudnet algorithm (??).~~ synergistic instrument algorithm Cloudnet (Griesche et al., 2020a).

2.2 BELUGA setup

The BELUGA system consists of a 90 m^3 helium-filled tethered balloon with a modular set-up of different instrument packages to explore the ABL between the surface and about 1500 m altitude. BELUGA can operate under cloudy and light icing conditions in the Arctic. Fixed to the balloon tether, a fast (50 Hz resolution) ultrasonic anemometer supported by an inertial navigation system measures the wind velocity vector in an Earth-fixed coordinate system, together with the virtual air temperature. Furthermore, barometric pressure, relative humidity, and the static temperature are measured with lower resolution (1 Hz). Relative humidity is measured with a capacitive humidity sensor, air temperature with a PT100 and a thermocouple. A second instrument payload is simultaneously fixed fixed simultaneously to the tether, measuring broadband terrestrial and solar net irradiances. Technical details on BELUGA, its instrumentation and operation during PASCAL, as well as data processing methods are given in by Egerer et al. (2019).

2.3 Humidity measurements under cloudy conditionsObservation period

Humidity and temperature measurements are challenging under cloudy and cold conditions. Specific humidity q is derived from measurements of air temperature T and relative humidity RH. Those parameters are obtained by regular radiosoundings (Vaisala RS92-SGP) and the BELUGA system with similar capacitive sensors ascending through the cloud layer, and therefore suffer from similar limitations. The main challenge is wetting of the sensors during the cloud penetration. A water film on the sensor might increase the response time (as the water needs to evaporate first) in the sub-saturated air above clouds during an ascent. This might significantly influence the air temperature and humidity measurements. A detailed discussion on wetting and icing problems of radiosondes is provided by Jensen et al. (2016), showing that wet-bulbing is an issue for the radiosonde type used during PASCAL. Artefacts of this process can thus be present in the humidity and temperature profiles as sampled by radiosondes. This is particularly relevant for studies of humidity inversions in the Arctic, most of which have made use of such radiosoundings. Because radiosondes penetrate the cloud layer from below, the impact of wet-bulbing is most pronounced when it leaves the cloud layer - which is unfortunately exactly the height range where the humidity anomaly is situated. This puts some doubt on radiosonde recordings of humidity inversions.

A simple and convincing test of the influence of possible wet-bulbing on the observations of SHIs is a measurement in the opposite direction, that is a descent from the free troposphere through the area with increased specific humidity into the cloud layer. This is not done with regular radiosoundings, but feasible for the BELUGA operation.

Figure **??** shows vertical profiles of RH, T and q as measured by both platforms (radiosonde and BELUGA) on 7 June 2017. The launch time of the radiosonde and the balloon differs by around 1.5 hours, which means that discrepancies in the measurements can also be attributed to changes in environmental conditions. Qualitatively, radiosounding and BELUGA measurements show a similar vertical structure. Both observations show a layer of increased specific humidity, hereafter referred to as humidity layer, between about 600 and 750 altitude. The increased specific humidity emerges from relative humidity remaining close to saturation within the temperature inversion, before decreasing to the free troposphere level well above the inversion base. The case on 7 June is selected as an illustrative example, because it is the only BELUGA flight of the

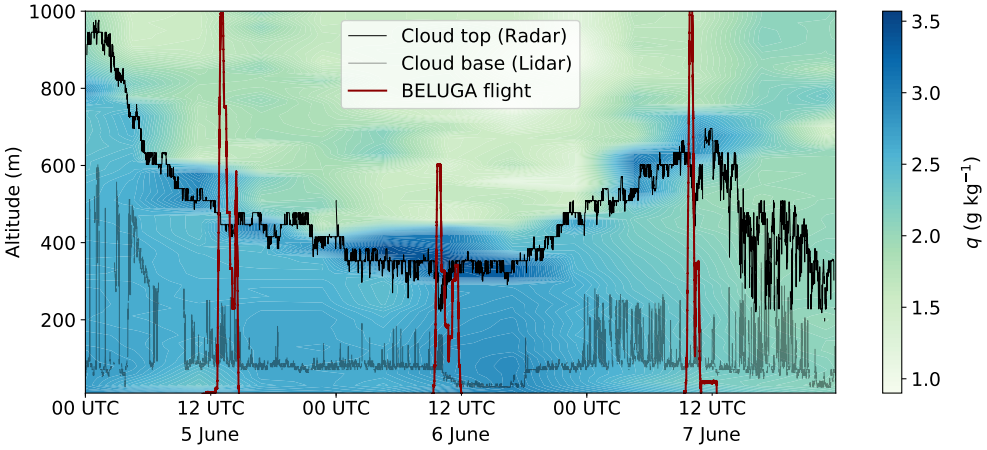

Figure 1. ~~Vertical profile~~ Temporal development of ~~relative humidity RH, Temperature *T* and~~ the specific humidity ~~*q* measured~~ vertical profile observed by ~~a radiosonde and BELUGA on 7 June 2017. The radiosounding was launched at 11:00 UTC, the balloon flew a continuous ascent and descent from 9:30 to 10:30 UTC~~radiosondes. The cloud ~~extent (~~radar-retrieved cloud top height is depicted as a black line; the cloud base height derived from ~~Cloudnet data)~~ the lidar nearfield-channel is ~~shown~~ indicated as ~~shaded area~~a grey line. The red lines represent the BELUGA flight profiles.

~~study period with a combination of a continuous ascent and subsequent descent. The descent also shows an increase of specific humidity, although the RH profile suggests reduced cloud height and thickness. The wet-bulbing effect cannot be quantified at this point, but despite the difference between ascent and descent the main vertical structure is similar. Hence, we conclude that the observation of the increased specific humidity is real and not the result of a measurement artefact.~~

~~The vertical cloud extent plays an important role for analyzing the vertical structure of specific humidity. The cloud boundaries in Fig. ?? are estimated from Cloudnet data (?) for the time of the balloon ascent and reflect the water and ice cloud. Unfortunately, the BELUGA instrumentation does not allow for in situ measurements of cloud liquid water to estimate the cloud boundaries more precisely.~~

3 ~~Case study~~

2.1 ~~Three-day period of a persistent humidity layer~~

~~A~~ The observational basis for this study is a persistent layer of increased specific humidity above a single-layer stratocumulus deck ~~is observed in~~ during the period between 5 and 7 June 2017. ~~This measurement case provides the observational basis for this study. Temporal development of the specific humidity vertical profile observed by radiosondes. The period 5 to 7 June 2017 exhibits a distinct layer of increased humidity above a low, single-layer stratocumulus. The cloud extent derived from Cloudnet data is depicted as black lines, the cloud base height derived from the *Polarstern* ceilometer data (Schmithüsen, 2018)~~

~~is indicated as a grey line. The red lines represent the BELUGA flight profiles. For this period, Fig. 1 shows~~ Figure 1 illustrates the temporal development of the vertical specific humidity profile derived from radiosonde measurements~~in combination with cloud boundaries and~~ . Cloud top and bottom and the time-height curves of the corresponding BELUGA flights are added for the investigated period. The BELUGA flights were conducted around noon on each of the three consecutive days. A local maximum ~~in specific humidity~~ of specific humidity is observed above the cloud top ~~is observed on all three days~~throughout almost the entire period, with a slight diurnal cycle peaking at noon~~and~~ , with a maximum specific humidity ~~around noon~~ on 6 June. It is worth noting that the observations show a well-defined layer of increased specific humidity, hereafter referred to as humidity layer, rather than a ~~humidity inversion~~ distinct and sharp SHI with only a slight decrease above.

~~Cloud boundaries~~ The cloud top and base height in Fig. 1 are estimated from ~~Cloudnet data. The comparison of cloud base height from the ceilometer onboard RV *Polarstern* and corresponding Cloudnet dataillustrates that the variability in the cloud boundaries is not represented in the Cloudnet data, but the temporal development is reproduced sufficiently by both methods.~~ the cloud radar and lidar (nearfield-channel) data, averaged over 30 s and with a vertical resolution of 30 m. Throughout the three-day period, cloud height and thickness decrease to a minimum at noon of 6 June, and thereafter increase again. The cloud is almost permanently of mixed-phase type with a maximum liquid water content (LWC) between 0.15 $\mathrm{g\,m^{-3}}$ and 0.6 $\mathrm{g\,m^{-3}}$ and an estimated ice water content (IWC) of about 0.03 $\mathrm{g\,m^{-3}}$ derived from Cloudnet data ~~(?, not shown here)~~(not shown here).

~~Balloon-borne vertical profiles for three noon-time measurement flights on 5, 6, and 7 June 2017. The altitude z is normalized to the temperature inversion base height z_i, which is defined as the lower boundary of the temperature inversion layer during the ascent. Potential temperature θ (a) and the specific humidity q (b) are normalized to their near-surface values. Panels (c) and (d) show horizontal wind velocity U and wind direction dd.~~

~~Figure 7 shows vertical profiles of the three BELUGA measurements during the 5–7 June period. Height is normalized by the base-height of the temperature inversion. To compare the ABL structure, the potential temperature θ and q are normalized by their near-surface values (~~Figure 1 depicts the high variability in cloud top and bottom heights. To illustrate the cloud situation around the BELUGA flights in more detail, Fig. ~~7a and 7b). All measurements show a similar vertical structure of θ and q. The ABL below the temperature inversion layer is slightly stably stratified. Above the temperature inversion, the thermodynamic stability is much increased compared to below the inversion. The potential temperature on~~ 2 shows the radar reflectivity and cloud boundaries for the particular three balloon flights. On 5 ~~June exhibits some variations above the inversion. On all days~~June, the cloud top height is approximately constant, whereas on 6 June the cloud top fluctuates between 350 m and 230 m in the course of the flight. During the 7 June flight, the cloud ~~is thermodynamically coupled with the surface layer , which manifests in the absence of a temperature inversion below~~ layer thins by 110 m starting from cloud top.

~~A distinct humiditylayer with slightly varying vertical relative thickness is observed on all days. The relative strength of this layer temporally decreases. The temperature inversion base coincidences with the base of the humidity layer. The vertical profiles of horizontal wind velocity and direction are shown in Fig. 7c and 7d. Throughout the period, the wind velocity increases inside the mixed layer from 2 to 7~~

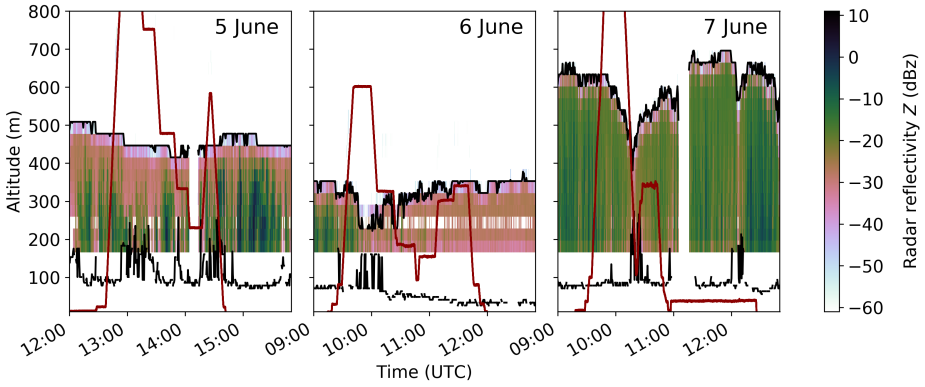

Figure 2. BELUGA flight profiles for 5, 6 and 7 June (red lines) with the radar reflectivity Z and cloud boundaries (black lines, as in Fig. 1).

3 Specific humidity measurements in a moist environment

3.1 Derivation of specific humidity

A cold and moist environment poses considerable challenges for the measurement of specific humidity. This can lead to measurement artifacts in the region of the SHI. Therefore, in this section we discuss the measurement of specific humidity with radiosondes and BELUGA as well as possible sources of error and their effects. Specific humidity q is used as a quantitative measure of the amount of atmospheric water vapor. It is derived from air temperature T and relative humidity RH using

$$q = \frac{R_\mathrm{d}/R_\mathrm{v} \cdot e_\mathrm{s}(T) \cdot \mathrm{RH}}{p - (1 - R_\mathrm{d}/R_\mathrm{v}) \cdot e_\mathrm{s}(T) \cdot \mathrm{RH}} \tag{1}$$

with the static pressure p, the ratio of specific gas constants of dry air and water vapor $R_\mathrm{d}/R_\mathrm{v} \approx 0.622$ and the ~~wind direction changes from southwesterly to northeasterly. The wind velocity is almost height-constant on 6 June, whereas on 5 and 7 June it gradually decreases above the mixed layer~~temperature-dependent saturation vapor pressure $e_\mathrm{s}(T)$. In this study, the measurements of RH and T are obtained by regular radiosoundings (Vaisala RS92-SGP) and observations with the BELUGA system. Both methods provide RH observations based on capacitive sensors, suffering from several limitations (Wendisch and Brenguier, 2013), which are discussed in the next section.

3.2 Error sources for humidity measurements

Several studies address the associated systematic errors of radiosonde RH and T measurements and identify three main sources: (i) wet-bulbing, (ii) solar heating, and (iii) time response errors.

3.3 ~~Vertical profiles of mean ABL parameters~~

~~For a more detailed study of the humidity layer, measurements close to the cloudtop and~~ (i) Wet-bulbing occurs when a water film develops on the sensor during cloud penetration, with subsequent evaporative cooling under sub-saturated conditions at higher altitudes after leaving the cloud. This effect leads to an overestimation of RH and an underestimation of T in the sub-saturated environment until the water film has completely evaporated. A detailed discussion of wetting and icing problems for radiosondes is provided by Jensen et al. (2016), showing that wet-bulbing is an issue for the radiosonde type used during PASCAL. The error induced by wet-bulbing is difficult to quantify (Dirksen et al., 2014).

(ii) When an RH sensor leaves the cloud and is exposed to direct solar radiation, it warms. This causes a radiation dry bias (measured RH is too low) of up to 5 % in the lower troposphere, depending on the solar zenith angle, altitude and temperature (Miloshevich et al., 2009; Wang et al., 2013). The error is corrected in the radiosonde data processing algorithm (Jensen et al., 2016). However, this correction is intended for cloud-free conditions. Solar heating also influences the temperature measurements (Sun et al., 2013). The effect on radiosonde temperature is negligible at low altitudes. For BELUGA, the temperature and RH sensors are shielded against direct solar radiation, but the sensor surroundings might warm and influence the measurements.

(iii) Furthermore, the time response for RH and T measurements is finite. Compared to the effects (i) and (ii), this part of the sensor behavior can be quantified. Assuming a first-order sensor response, the time dependence of a measured signal $x_\mathrm{m}(t)$ (RH or T in our case) is given by

$$\frac{\mathrm{d}x_\mathrm{m}}{\mathrm{d}t} = 1/\tau\,(x_\mathrm{a} - x_\mathrm{m}) \tag{2}$$

with a time constant τ and the ambient ("true") signal x_a. The time constant τ depends on the temperature and ventilation of the sensor with larger response times at low temperatures and small flow speeds. The time-lag corrected signal is

$$x_\tau = \frac{\tilde{x}_m(t) - \left[\tilde{x}_m(t-\Delta t)\cdot e^{-\Delta t/\tau}\right]}{1 - e^{-\Delta t/\tau}} \tag{3}$$

with Δt being the time step between two consecutive measurement points (Miloshevich et al., 2004). Here, we assume that the time-corrected value (index τ) is equal to the ambient value x_a. The tilde in Eq. 3 represents the low-pass filtered, measured time series. Although radiosonde data processing routines consider the time response error, fast humidity changes in cold conditions are still affected (Smit et al., 2013; Edwards et al., 2014).

All three error sources might be relevant for observational studies of SHIs in the Arctic. This holds particularly true for observations based on radiosoundings, because they first penetrate the cloud layer before reaching the temperature inversion and SHI. Furthermore, in the presence of strong humidity and temperature gradients – as observed just above the cloud layer – the impact of time lag errors is most pronounced and gradients are significantly smoothed when neglecting this effect.

3.3 Estimating the time constants of the humidity sensor

We determine the time constants for the BELUGA humidity sensor in laboratory experiments by analyzing the sensor response to a step-like change of the surrounding thermodynamical parameters. The sensor is brought from a calm and saturated

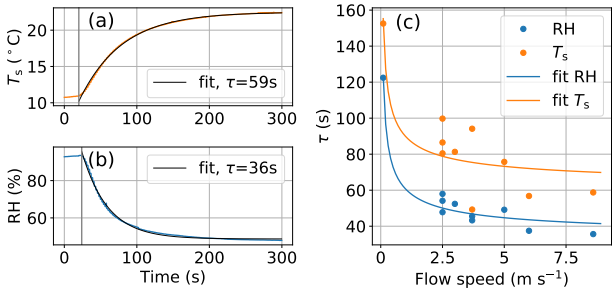

Figure 3. Time response of the humidity sensor to a step function experiment: (a) sensor-internal temperature T_s and (b) RH at 8.6 m s^{-1} with fitted time constants τ. Panel (c) shows the time constants depending on the flow speed. A root fit function is added to the values.

environment into a sub-saturated airstream with constant T and RH. The flow speed of the ~~temperature inversion are analyzed. Figure 8, Fig. 9 and Fig. 10 a–d each show vertical profiles of mean ABL parameters measured by BELUGA on the 5, 6 and 7 June, respectively. The cloud top height is indicated as a vertical height range instead of a sharp boundary height. Cloud top variability within this region can be caused by spatial or temporal cloud heterogeneity, and by the use of different measurement methods. The vertical height range shown in the figures expresses the spread in cloud top height among Cloudnet data, RH measurements and the height of maximum radiative cooling, which is supposed to be located at cloud top (Wood, 2012).~~ sub-saturated air is varied between 2 m s^{-1} and 9 m s^{-1}. In addition to RH, the sensor provides a measure for the internal sensor temperature T_s, which is determined by a PT-1000.

~~Boundary layer observations around cloud top on 5 June 2017: Vertical profiles of (a) potential temperature θ and RH, (b) specific humidity q, (c) terrestrial heating rate $\partial T/\partial t$, (d) horizontal wind velocity U and vertical wind velocity w, (e) local dissipation rate ε and turbulent kinetic energy TKE and (f) virtual sensible heat flux H. Small red dots represent flux estimates on the slant profile, big black dots on constant altitude segments. Red big dots represent constant altitude fluxes based on high-pass filtered data. The cloud is shown as shaded area, the cloud top height range as hatched area.~~ Figure 3a and 3b show an example for the time response of the humidity sensor on BELUGA. The time constants τ_{RH} and τ_{T_s} are obtained from an exponential fit to the response function at a constant flow speed of 8.6 m s^{-1}. Figure 3c summarizes the resulting time constants for different flow speeds. The time constant of a temperature and RH sensor is influenced by the heat and moisture transfer, which scale with the flow speed $\propto 1/\sqrt{U}$ (e.g., Bruun, 1995, for heat transfer). Based on this relationship, a least-square fit to the observations yields the τ values depending on the flow speed. For flow speeds typical for atmospheric observations, we estimate time constants of $\tau_{T_s} \approx 70$ s and $\tau_{RH} \approx 50$ s. Similar to Miloshevich et al. (2004), we multiply the estimated time constant with a factor of 0.8 before the time series reconstruction to avoid potential over-correction.

For the reconstruction of the time series, τ is evaluated for each measurement point with the measured wind velocity by applying Eq. 3. Low-pass filtering in Eq. 3 is realized by a Savitzky-Golay filter with a window length of τ. This low-pass filtering is necessary to avoid amplification of gradients caused by signal noise or digitization steps (Miloshevich et al., 2004). The time-response correction is applied to the RH and the internal temperature data. The time constant for the T measurements

based on the thermocouple on BELUGA was found to be below 1 s (Egerer et al., 2019) and, thus, has a minor influence on the vertical temperature profile compared to the humidity observations.

~~Potential temperature inversion (TI) and humidity layer (HL) characteristics for 5, 6 and 7 June 2017. 5 June~~

3.4 Sensitivity of q to the RH and T profile

We perform sensitivity studies to analyze how the three error sources (cf. Sect. 3.2) for T and RH measurements combine and influence the derivation of q. The errors are simulated as T and RH deviations from a synthetic reference case (grey line in Fig. 4), which represents a simulated measurement of a temperature inversion combined with a decrease of RH. The temperature linearly increases by 6~~June 7 June TI: ΔT () 11 6.8 7 TI depth () 90 40~~ K in the 200 m thick inversion layer, whereas RH linearly decreases from 100~~TI gradient ()0.12 0.17 0.07 TI base height () 430 290 575 HL: Δq () 1.1 1 0.7 HL depth () 150 50 135 Characteristics of~~ % to 40 % in the same height range. With these synthetic profiles, the specific humidity decreases monotonically within the inversion layer without reproducing a SHI.

In a first set of simulations, we consider the influence of possible measurement errors in the temperature inversion ~~layer and~~ region for the ~~humidity layer are summarized in Table **??**. The strongest temperature difference of 11~~ T and RH sensor separately. That is, only one sensor will be influenced by an increased or decreased signal, while keeping the other sensor reading at the reference value. The magnitude of the simulated deviations (Fig. 4a and 4b) is arbitrary, but the qualitative profile of the effected signal is according to the error sources, as discussed in Sect. ~~is found on 5 June 2017, decreasing to 7 for the following two profiles. The temperature inversion layer depth decreases from 90 to 40 and afterwards increases again to 100 throughout the period. This results in a temperature gradient between 0.07 and 0.17 , with a maximum on 6 June. The strength of the humidity layer slightly decreases from 1.1 to 0.7 . Starting with a depth of 150 on 5 June, a minimum in humidity layer depth of 50 is observed on 6 June.~~ 3.2.

~~On 5 June, the cloud layer is capped by the temperature inversion, whereas the cloud top tends to penetrate slightly into the inversion on 6 and 7 June. This extension of~~ The effect of the four errors (T or RH too high or too low in the temperature inversion region) on the specific humidity profile is shown in Fig. 4c. An artificial humidity layer above the ~~cloud layer into the temperature inversion layer is common for Arctic clouds (e.g. Pleavin, 2013). Due to the uncertainties in estimating cloud top height, it ischallenging to quantify how deep the cloud penetrates into the inversion.~~ cloud can emerge when the RH sensor overestimates the moisture due to wet-bulbing (but keeping the temperature sensor unaffected), or when the temperature sensor is heated in the inversion region but the humidity sensor is unaffected. Vice versa, q shows a deficit compared to the reference when one of the sensors indicates underestimated values compared to the reference scenario. If a single phenomenon affects both the temperature and RH sensor (e.g., wet-bulbing results in overestimated RH and underestimated temperature), the errors in the determination of q have an opposite effect and, therefore, the overall error in q is reduced.

~~Same as Fig. 8, but for 6 June 2017.~~

~~Same as Fig. 8, but for 7 June 2017. No constant altitude segments were recorded.~~

~~The maximum terrestrial (longwave) radiative cooling (a minimum in the terrestrial heating rate $\partial T/\partial t$) coincidences with the coldest point of the temperature inversion – the inversion base.We observe terrestrial cloud top cooling rates between -6~~ As

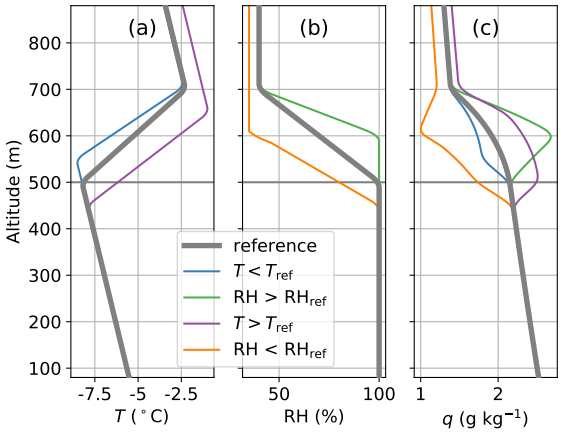

Figure 4. Sensitivity of the vertical q profile to a deviation of T and RH compared to a reference case (grey line). Only one parameter (T or RH) experiences a deviation, the other parameter is unchanged.

a second step, we simulate the influence of different time constants τ_{RH} and τ_T for the RH and temperature measurements. The same reference case as above is imposed with a lagging T and RH signal in both upward and downward direction, representing ascent and descent. Figure 5 shows synthetic measurements assuming two combinations of time constants for both sensors ($\tau_{RH} = 40$ s combined with $\tau_T = 60$ s and ~~8~~$\tau_T = 1$ s). The values for τ are based on the results of Sect. ~~on all days. In all three cases, the maximum of specific humidity is located clearly above the cloud layer~~ 3.3 without correcting the time-lag error. If both time constants are similarly high ($\tau_{RH} = 40$ s and ~~above the cloud top cooling region.~~ $\tau_T = 60$ s), the resulting q does not change significantly in magnitude, but the vertical structure shifts upwards or downwards (Fig. 5c). If $\tau_{RH} \gg \tau_T$, q is overestimated during the ascent, producing an artificial SHI, but underestimated during the descent.

~~The transition from the cloud to free troposphere is characterized by a more or less pronounced decrease of horizontal wind velocity, which corresponds to vertical wind shear. An increase in the horizontal wind velocity in the cloud layer is observed on 5 and 7 June. The wind velocity at cloud top decreases by 2 on 5 June and by 5 on 7 June.On 6 June there is only a local (20 vertically extending)decrease in horizontal wind velocity just above the cloud of below 1 . In all cases, the fluctuations of vertical wind w are pronounced inside the cloud compared to above the cloud. The gradient Richardson number Ri is greater than one for all days~~ As a result of these sensitivity studies, the error in q is reduced when both the temperature and humidity sensors are affected by the same error source (e.g.~~Ri $\approx$ 5 on 6 June), which means that wind shear at cloud top allows only little turbulence.~~ , wet-bulbing on both sensors), and when both sensors have comparable time constants. Under these conditions, a detected SHI can be considered most likely as real and does not need to be interpreted as an artifact.

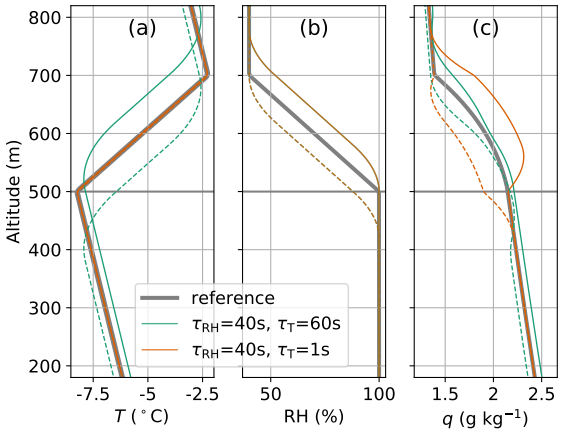

Figure 5. Sensitivity of the vertical q profile to combinations of different time constants τ_{RH} and τ_T. Solid and dashed lines represent the ascents and descents, respectively.

3.5 ~~Turbulent transport from the humidity layer into the cloud~~SHIs measured with BELUGA and radiosondes: Natural feature or artifact?

3.5.1 ~~Turbulent ABL parameters~~

~~Of key importance for understanding the impact of humidity layers on the underlying cloud layer is to gain insight into the coupling between both layers, as expressed by the vertical transport of humidity between them. To this purpose the profiles of various turbulence-related variables are analyzed. Use is made of a technique to estimate the local dissipation rate ε and local turbulent kinetic energy TKE from the slant profile data obtained from BELUGA observations, as described in detail by Egerer et al. (2019). In the present cases, the local turbulence, as described by ε and TKE, is most pronounced in the cloud layer for all days with typical values of $\varepsilon \sim 10^{-3}$ and TKE ~ 0.03 (Fig. 8e, 9e and 10e)~~

A simple and convincing test of the possible influence of the error sources on the SHI observations is profiling in opposite direction, that is a descent from the free troposphere through the SHI into the cloud layer. This is commonly impossible in case of standard radiosoundings, but feasible for the BELUGA observations. ~~For 7 June (Fig. 10e), with increased wind velocity, a clear maximum of ε is evident just below cloud top, which is where the terrestrial radiative cooling rate is also at its maximum. At cloud top~~

Figure 6 shows vertical profiles of RH, T, and q as measured by radiosounding and BELUGA on 5 June 2017. Qualitatively, the measurements of both platforms show a similar vertical structure with a sharp temperature inversion capping the cloud layer. The cloud top (estimated from the downward terrestrial irradiance measured for the BELUGA ascent and descent) is situated in the height region of the temperature inversion base. However, the cloud top height derived from radiation observations should be treated with caution due to the vertical separation of the radiation and thermodynamic sensors by about 20 m, corresponding

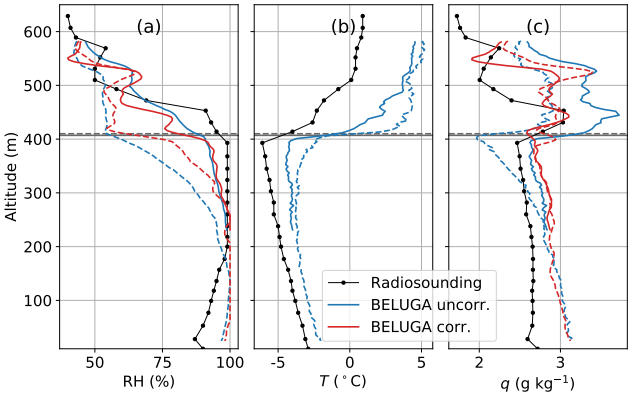

Figure 6. Vertical profiles of (a) relative humidity RH, (b) temperature T and (c) specific humidity q measured by a radiosonde and BELUGA on 5 June 2017 (second profile). RH and q for BELUGA are shown before and after the corrections. The radiosounde was launched at 16:50 UTC, the balloon flew a continuous ascent and descent from 14:15 to 14:40 UTC. The cloud top (from BELUGA radiation data) is shown as horizontal lines. Solid and dashed lines represent the BELUGA ascent and descent, respectively.

to a temporal shift between the observations of about 20 s during profiling. In the course of the measurement period of almost two hours, the temperature inversion base and the cloud top remain at an almost constant altitude. The radiosonde observation shows a layer of increased q between 400 m and 550 m altitude just above the temperature inversion base. The increased specific humidity emerges from RH remaining high within the temperature inversion~~layer, c decreases to the low-turbulent~~, before decreasing to the free troposphere level ~~. This transition appears gradual, which shows that the humidity layer is not completely decoupled from the cloud layer. Instead, both layers are connected by turbulent mixing.~~ well above the inversion base.

3.5.1 ~~Eddy covariance fluxes~~

~~To investigate the vertical moisture transport, the vertical turbulent moisture flux (or latent heat flux), which is proportional to $\overline{w'q'}$ needs to be quantified.However, this requires fast humidity measurements, which are not available with our instrumentation.Alternative we argue that an estimate of the turbulent virtual heat flux~~

$$H = \overline{\rho} \cdot c_p \cdot \overline{w'\theta'_v}$$

~~provides an indication for the direction of the turbulent energy fluxes. Here, θ_v is~~ Before comparing the q measurements from the radiosonde to BELUGA observations, we illustrate the effect of the applied RH correction and the consequences for the q profile. Figure 6a shows the ~~virtual potential temperature (as measured by the ultrasonic anemometer), $\overline{\rho}$ is the mean air density and $c_p = 1005$ the specific heat capacity of air. Fluctuating parameters are marked with a prime, time averages with an overline.Both temperature~~ uncorrected and time-response corrected RH for an ascent and descent. The uncorrected RH ascent profile deviates strongly from the descent in the cloud top region. While descending through the cloud, the sensor requires

150 m height difference for rising from 55 % to 95 % RH. The RH hysteresis around cloud top is visible as a systematic deviation in all observed flight data (not shown here). A comparison to Fig. 4 and Fig. 5 (orange lines) suggests that the major part of the error is due to a slow RH sensor. Furthermore, the sensor is too warm compared to the environment on the descent, as humidity is reduced and the vertical structure is shifted slightly downwards. After applying the time lag correction, the RH profile shows a significantly reduced difference between ascent and descent. The remaining difference is qualitatively consistent with the temperature observations as shown in Fig. 6b. The temperature profiles show a warming of the cloud top and inversion region between 300 m and ~~humidity exhibit similarly strong gradients above the cloud layer. Lilly (1968) applied the ratio of the heat flux to the potential temperature difference across the inversion for defining the entrainment velocity w_e:~~

$$w_e = -\frac{\overline{w'\theta'}|_{z_i}}{\Delta\overline{\theta}}.$$

~~This relationship can be applied to any conserved variable at the ABL top, such as~~ 500 m during the descent leading to a reduced RH.

The "uncorrected" specific humidity in Fig. 6c is calculated from the uncorrected RH and the temperature measured with the fast-response thermocouple. The resulting q ~~(de Roode and Duynkerke, 1997). With a positive w_e and similar θ_v and~~ profiles show a SHI on the ascent and the descent of the BELUGA flight with a similar structure and location compared to the radiosonde data. The q ~~gradients, we can assume that the fluxes of heat and moisture will point in the same direction. This assumption is further discussed in Sec. ?? and in combination with the LES results.~~ profile as observed during the descent is shifted to lower q values in the region of the hysteresis of the uncorrected RH.

~~Vertical profiles of turbulent fluxes can be estimated by (i) measurements averaged over time periods at different constant altitudes, or (ii) by averaging the collected data over altitude segments on a continuous vertical profile (slant profiles) (Egerer et al., 2019). Slant profiles describe the instantaneous vertical structure of turbulent fluxes, but with a reduced statistical significance of the absolute value. The values strongly depend on the vertical extent of the selected sub-record.~~ The corrected q results from the RH and the sensor-internal temperature T_s after correcting both signals for the ~~horizontal wind velocity and on the type of implicit high-pass filtering. Another challenge is~~ time lag error according to Eq. 3. The internal temperature T_s is measured inside the housing of the RH sensor, which has a high diffusivity for water vapor. We argue that using T_s should be preferred instead of using the thermocouple readings because RH and T_s have similar time constants, and RH is measured at T_s instead of the temperature of the ~~high-pass filtering itself in regions of strong or rapidly changing gradients, which is typical for~~ atmospheric environment. The ambient temperature and T_s slightly differ due to thermal inertia of the sensor housing.

After applying the corrections, the maximum value of the SHI, as observed during the BELUGA ascent, is reduced by about 0.6 g kg^{-1} compared to the uncorrected q maximum. After correction, all BELUGA profiles and the radiosonde data exhibit the SHI with similar structure and amplitude. The three profiles are consistent with each other, which suggests that the observed SHI is a natural feature instead of an instrumental artifact. This conclusion does not generally rule out the possible influence of error sources such as wet-bulbing or solar heating, but these errors are not the source for the SHIs observed by BELUGA or other radiosonde-based studies.

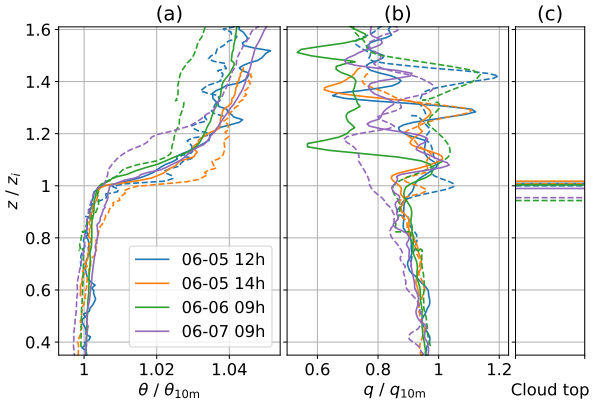

Figure 7. Balloon-borne vertical profiles of (a) potential temperature θ, (b) specific humidity q and (c) cloud top for four ascents (solid lines) and descents (dashed lines) on 5, 6, and 7 June 2017. The altitude z is normalized to the temperature inversion base height z_i. Potential temperature θ and the specific humidity q are normalized to their near-surface values. The cloud top (derived from the irradiance profile) is shown as horizontal lines for the ascent (solid) and descent (dashed). The profiles are named after the day and the hour of the start time (cf. Fig. 2).

4 Vertical profiles of mean ABL parameters

4.1 Comparison of normalized temperature and humidity profiles

One of the governing questions of this analysis is to understand how the SHI relates to the general ABL structure and, in particular, to the temperature inversion~~height range. In those regions, the choice of the filter type is crucial and can produce artificial fluctuations, which dominate the flux estimate. Therefore, the fluxes in the cloud top region are not shown for the measurements conducted on 5~~. Figures 7a and 7b show vertical profiles of potential temperature θ and specific humidity q recorded in the period of 5–7 June. ~~For flux estimates derived from constant altitude flight patterns, the time records are detrended to define the turbulent fluctuations. For the slant profiles, a high-pass filter of Bessel type is applied. The filter window is adjusted to the daily conditions of cloud thickness and horizontal wind, resulting in a window between 47~~Both parameters are normalized to their near-surface values and plotted in relation to the base-height of the temperature inversion z_i. The cloud top height is shown in Fig. 7c as reference.

All measurements show a similar vertical structure of θ. Below the temperature inversion base z_i, the mixed layer is almost neutrally stratified and gradually becomes more stable starting just below the capping temperature inversion. Above this inversion, the thermodynamic stability exhibits more variability and is higher compared to the mixed layer. This applies to the comparison of different profiles, but also to the variability within an individual profile. No systematic difference between ascents and descents is visible. The ABL is thermodynamically coupled to the surface, which makes normalizing to surface values meaningful.

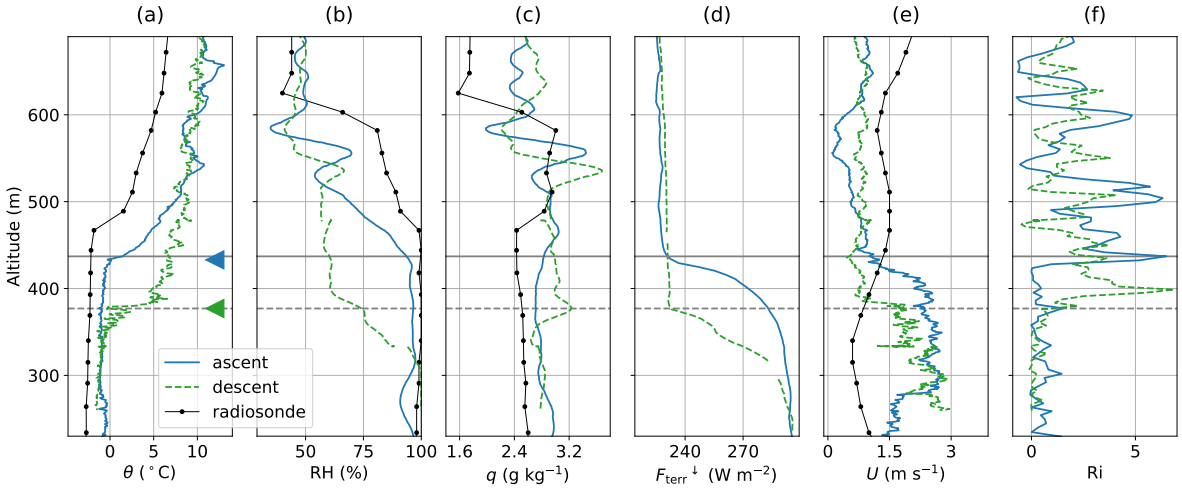

Figure 8. Boundary layer observations around cloud top on 5 June 2017, first profile: Vertical profiles of (a) potential temperature θ, (b) RH, (c) specific humidity q, (d) downward terrestrial irradiance $F_{\text{terr}}{}^{\downarrow}$, (e) horizontal wind velocity U and (f) Richardson number Ri for BELUGA ascent and descent and the radiosonde launched at 11 am. The triangles indicate where z_i is defined. The cloud top is shown as horizontal lines (solid for ascents and dashed for descents).

Within the mixed layer below z_i, specific humidity slightly decreases with height, but increases when reaching z_i. Above z_i, the normalized specific humidity exhibits more variability compared to the normalized temperature. The descent of 06-07 09h does not show one clear temperature inversion, but some variability in θ with two smaller "steps". We define z_i at the lower step, with the SHI base being located clearly above at the upper step at $z \approx 1.2 \cdot z_i$. For this case, a deficit in q is observed below the SHI, which is plausible because between ascent and descent cloud top decreased to about $0.95 \cdot z_i$.

For most profiles, the cloud top coincides with z_i and the increased humidity is observed above the cloud layers. Only for two profiles (both descends on 5 June), the lower bound of the SHI is located already below the cloud top. We do not find clouds penetrating into the temperature inversion, although such situations have been frequently observed in previous studies (e.g., Pleavin, 2013; Sedlar et al., 2012; Sedlar and Shupe, 2014; Shupe et al., 2013; Brooks et al., 2017). However, two of the descent profiles (06-06 09h and ~~110~~06-07 ~~. This corresponds to a spatial scale of about 100 to 400 , depending on the horizontal wind velocity, and is of the same order as the vertical extent of the cloud layers. Additionally, the same high-pass filter is applied to the constant altitude records for a comparison to the slant profile fluxes.~~ 09h) show situations, where the cloud top decreased between ascent and descent, and the SHI is vertically separated from the cloud top.

4.2 Cloud top variability versus SHI height

~~It is still challenging to obtain vertical profilesof turbulent fluxes. Slant profiles suffer from a short averaging time for flux estimates and omit lower-frequency contributions. Estimating turbulent fluxes on constant altitude segments is statistically~~

~~more robust, but more difficult to obtain. Further, measuring in a constant altitude does not ensure stationary conditions because of the high temporal variability of the ABL and~~ The cloud top variability, here defined as the cloud top height difference between ascent and subsequent descent for each profile, is related to z_i and the lower boundary of the SHI. For all three days, a descending cloud top is observed in the course of the ~~influence of possible gravity waves. It is beyond the scope of this work to discuss all uncertainties of estimating turbulent fluxes (a discussion can be found e.g. in Lenschow et al., 1994). Instead, the presented results should be considered as a qualitative indication of the direction of vertical moisture transport.~~

~~During the three-day period of measurements analyzed here, the virtual sensible heat fluxes inside the cloud layers are predominantly positive (~~profile with a cloud top height difference of 50 m to 100 m between the ascent and subsequent descent. This cloud top variability is indicated by irradiance and thermodynamic measurements of the BELUGA system and also confirmed by radar reflectivity (cf. Fig. 2). In order to illustrate the relation of cloud top height, SHI, and other ABL parameters, Fig. 8~~f, 9f and 10 f). Values from constant altitude records are up to 20 for~~ , 9, and 10 show profiles of mean θ, RH, q, downward terrestrial irradiance $F_{\mathrm{terr}}{}^{\downarrow}$, horizontal wind velocity U, and Richardson number Ri as measured during ascents and descents on 5~~June, and up to 10 for~~ , 6 ~~June. On~~ and 7 ~~June, no data from constant altitude measurements are available, but the slant profile fluxes reach up to 5 in the cloud. Above the temperature inversion layer, the turbulent fluxes vanish and are close to zero during the entire three-day period~~June, respectively. We analyze only continuous profile data without longer breaks at certain heights for the first profile of each day. The cloud top height is defined by the discontinuity of the $F_{\mathrm{terr}}{}^{\downarrow}$ profile and marked with horizontal lines, whereas z_i is indicated with triangles. The Richardson number is the ratio between thermodynamic stability and wind shear and, therefore, a measure for the ability of turbulence generation (Ri $\lesssim 1$) or dissipation (Ri $\gtrsim 1$).

~~On 6 June , a negative virtual sensible heat flux of -15 is observed close to~~ On 5 June (Fig. 8), z_i lowers from 430 m to 380 m in the course of the ~~cloud top, suggesting vertical mixing of air from the humidity layer into the cloud top layer. This is the only record with observations at constant altitude inside the inversion layer~~BELUGA flight. The temperature difference across the inversion of $\Delta\theta \approx 9$ K, which is ~~hard to locate exactly during the measurements.~~

~~The time series for the flux calculation parameters in this altitude are shown in Fig. 13. The temperature record shows rapid variations of up to 3 and exhibits structures with a typical time scale of a 30–50 .~~ also the strongest observed during our flights, stays constant during ascent and descent. The ~~temperature variations are detected by different sensors (PT100, thermocouple and the Sonic anemometer), which excludes an instrument artefact. The magnitude of the temperature structures is about half of the temperature difference across the inversion of $\Delta\theta = 6.8$.~~ RH decreases within the temperature inversion, accompanied with an increase in q above z_i of about 0.25 g kg^{-1} (ascent) and 0.5 g kg^{-1} (descent). The radiosonde, launched around two hours prior to the BELUGA flight, shows a higher z_i but qualitatively a similar vertical structure of θ, RH, and q. The cloud top agrees well with z_i for the ascent and descent. The horizontal wind velocity U is around 2 m s^{-1} inside the cloud layer and decreases to 1 m s^{-1} in the free troposphere, resulting in horizontal wind shear. During the ascent, the wind shear zone is clearly located below z_i with a sudden increase of Ri to values greater than 1 above z_i and cloud top. During the descent, the strongest wind shear is observed around z_i, and the resulting increase of Ri is slightly above z_i. This vertical shift suggests a slightly stronger turbulent coupling between cloud top and the SHI above, as compared to the ascent.

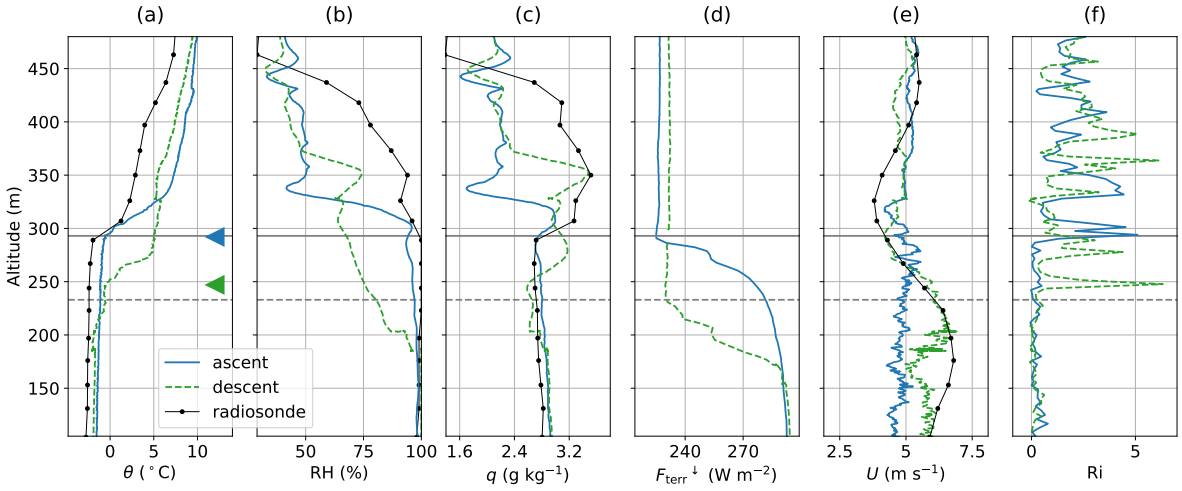

Figure 9. ~~Time series of (a) virtual potential temperature θ_v, (b) vertical wind w and (c) covariance $\theta_v' w'$, (d) yaw angle and (e) barometric pressure p_b~~Same as Fig. ~~The data are recorded on~~ 8, but for 6 June 2017 ~~on the constant altitude segment in 302 ±3 altitude and used for the flux calculation in Fig~~(first profile). ~~9.~~

The ~~temperature fluctuations might result either from the instrument moving up and down in the temperature inversion or from the air mass oscillating around the instrument. The barometric pressure p_b spans a range of 0.6 throughout the entire time series, which corresponds to altitude variations of about 5 . The measurement altitude for the second part of the record varies only in the range of ±~~ general ABL structure observed on 6 June (Fig. 9) in terms of the profiles of θ, RH, and q is quite similar to the 5 June observations, showing a decreasing cloud top height during the balloon operation. Here, z_i decreases from 290 m during the ascent to about 230 m during the descent. The radiosonde, launched 1.5 ~~hours after the BELUGA flight, shows a similar z_i as the balloon ascent, indicating that z_i and cloud top recover between BELUGA descent and radiosounding. This is in agreement with the radar observations in Fig. 2. The lower bound of the SHI with $\Delta q \approx 0.3\,\mathrm{g\,kg^{-1}}$ on the ascent and $0.7\,\mathrm{g\,kg^{-1}}$ on the descent is coupled to z_i in both cases. On the ascent, z_i coincides with the cloud top, whereas during the descent the cloud top is almost 20 m . Based on~~ below z_i. However, the temperature gradient ~~of 0.17 , this altitude variation corresponds to a temperature change of ± 0.3 . Therefore, the observed temperature structures with amplitudes~~ is smoother compared to the ascent, which leads to a less clear determination of z_i. The humidity structure above the cloud layer observed by the radiosonde exhibits a distinct SHI with a lower bound coupled to the temperature inversion. Peak values of q are comparable with BELUGA observations made during the descent. The horizontal wind velocity is about 5 $\mathrm{m\,s^{-1}}$ and almost height-constant for the entire ascent, but increases by about 2 $\mathrm{m\,s^{-1}}$ inside the cloud layer during the descent. The radiosonde provides a similar picture as the balloon descent. For the ascent, the sharp increase of Ri is connected to z_i, whereas for the descent this increase of Ri is – similar to the previous day – about 20~~times higher are mainly not caused by altitude variations, but instead correlate with changes in the yaw angle of about 10°, meaning with a change in wind direction. There are no similar~~

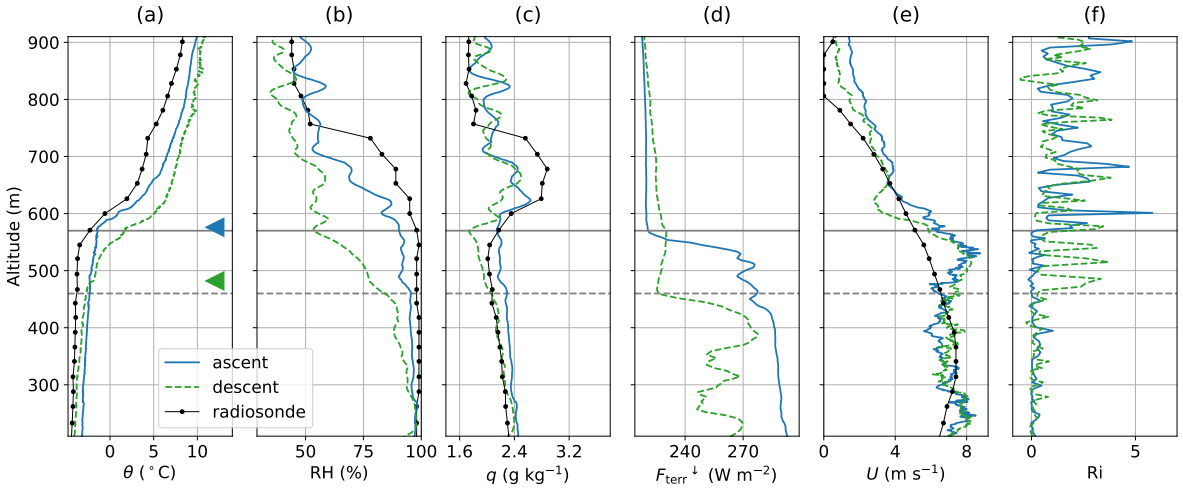

Figure 10. Same as Fig. 8, but for 7 June 2017.

~~structures in the record of the horizontal wind speed (not shown in~~ m above cloud top, allowing for some turbulent exchange between the cloud and the SHI above.

On 7 June, a clear SHI develops with a lower boundary at around 580 m, which is similar in the two BELUGA and the radiosonde profiles (Fig. ~~13).~~

~~A more plausible explanation for the observed temperature structures are external gravity waves (as waves may alter the wind direction), which are frequently observed in temperature inversion layers. Deardorff et al. (1969) observed convectively induced waves at the interface of a mixed layer and a stable layer in water tank experiments. Further, Driedonks and Tennekes (1984) reported intermittent turbulence for the entrainment zone of a convective ABL. Gravity waves oscillate with the Brunt–Väisälä frequency~~

$$N = \sqrt{\frac{\mathrm{g}}{\theta} \cdot \frac{\partial \theta}{\partial z}}.$$

~~In our case, this results in $N \approx 0.08$ and a wave period of $2\pi/N \approx 78$. This is around three times the observed wave period of ~ 25 to 30 in Fig. 13~~10). For the BELUGA ascent and the radiosonde profile, this boundary agrees well with z_i and cloud top (for the radiosonde data cloud top can be roughly estimated from the RH profile). The radiosonde profile and BELUGA ascent are shifted in time by about 70 min and the remarkable match in z_i should not be over-interpreted. For the BELUGA descent, the thermal stratification changes again (similar to the previous days). The temperature inversion weakens and z_i is shifted downward by about 110 m to 480 m, together with the cloud top. Thus, the cloud top and the SHI base are separated by 110 m on the descent. The terrestrial irradiance inside the cloud layer fluctuates strongly, especially on the descent, which suggests a patchy cloud with cloud holes. The horizontal wind velocity agrees qualitatively for all three profiles. Inside the ABL, a higher wind velocity of around 6 $\mathrm{m\,s^{-1}}$ is observed with the BELUGA observations, showing a local maximum of

$8\,\mathrm{m\,s^{-1}}$ slightly below z_i. Above this maximum, U gradually decreases to $2\,\mathrm{m\,s^{-1}}$ in the free troposphere. According to the Richardson number, wind shear limits turbulence above the cloud top for both ascent and descent.

~~The observed temperature structures violate the classical Reynolds decomposition $x'(t) = x(t) - \overline{x}$, which requires $\overline{x'} = 0$ for a sufficient averaging time~~To resume, we observed mean profiles of several cases where cloud tops coincide with z_i and the SHI base. Although some cloud tops show more or less strong horizontal wind shear, the stabilizing effect of the temperature inversion leads to a sudden increase in Ri just above the cloud layer, which suggests a rather low turbulent exchange with the humidity layers above. However, ~~this is a major precondition for the flux calculation. The calculated amplitudes of the temperature fluctuations strongly depend on how the averaging is carried out. In Fig. 13, θ_v'~~for one case a special situation provides a new aspect of this phenomenon: z_i and cloud top height had decreased while the humidity layer remains at its vertical position, leading to a gap between cloud top and SHI.

5 Turbulence at cloud top and around the SHI

Concerning the question of how the humidity and cloud layer interact and to what extent these layers exchange energy by turbulent transport, we analyze the profiles of basic turbulence parameters (Sect. 5.1) and turbulent energy fluxes (Sect. 5.2). In Sect. 5.1 we examine in more detail the transition between the SHI and cloud top.

5.1 Vertical profiles of turbulent energy and dissipation

The vertical distribution of turbulence parameters, such as local dissipation rate ε and the turbulent kinetic energy TKE, provide a first insight into the coupling between the cloud layer and the SHI. The local ε values are derived from second order structure functions by applying inertial subrange scaling as described by Egerer et al. (2019). Different from this study, here ε is calculated from non-overlapping, ~~w' and $\theta_v' w'$ are calculated by subtracting the linear trend (black curves) and by high-pass filtering with a Bessel filter with a filter time window of 47 (red curves). The filter parametersare the same as applied for filtering on the slant profile. The results for the fluxes estimated from filtered time series observed at constant heights are added as red dots in Fig. 8f and 9f. When applied to all constant altitude time series, the filter algorithm reduces the magnitude of the estimated fluxes, but the vertical structure remains. Magnitude and vertical structure are comparable to the results of the slant profile.~~ $2\,\mathrm{s}$ sub-records yielding a vertical resolution of about $2\,\mathrm{m}$. Regions without inertial sub-range scaling are excluded. Turbulent kinetic energy ($= 0.5 \cdot {u_i}^2$) is calculated in a rolling $50\,\mathrm{s}$ window. The observed TKE noise level is about $0.005\,\mathrm{m^2\,s^{-2}}$ and is usually reached at $z/z_i \gtrsim 1.1$.

~~The cloud top virtual sensible heat flux on~~

Figure 11 shows ε and TKE for each first profile of 5, 6 ~~Juneresults mainly from temperature fluctuations, rather than from wind velocityfluctuations. Independent from the filter settings,~~ and 7 June as a function of normalized height (the descent of 5 June is excluded due to data issues). The cloud and humidity layers are shaded for reference. For the presented cases, turbulence is most pronounced in the upper cloud layer and around cloud top with typical values of $\varepsilon \sim 10^{-3}\,\mathrm{m^2\,s^{-3}}$ and

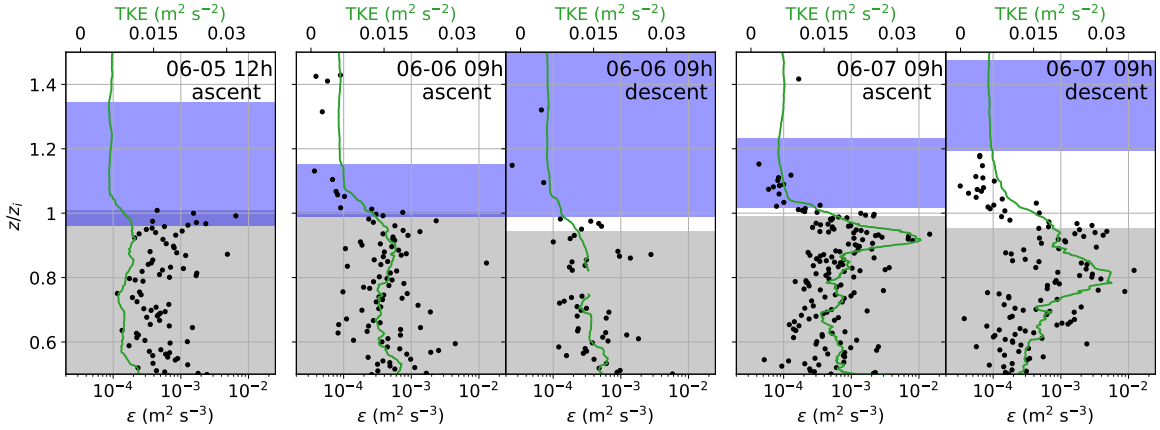

Figure 11. Vertical profiles of local dissipation rate ε and TKE for the first ascent and descent of 5, 6 and 7 June 2017. The height is normalized by the temperature inversion base z_i. The region of increased specific humidity is marked as blue shading, the cloud layer as grey shading.

TKE $\sim 0.02\,\mathrm{m^2\,s^{-2}}$. For 5 and 6 June, the turbulence intensity is rather constant in the cloud. For 7 June, with increased wind velocity, a maximum of ε is evident just below cloud top.

Figure 11 also illustrates how the SHI and cloud layer are either separated or overlap, and how they are connected by turbulent motion. At a certain height level, ε decreases to the low-turbulence free troposphere level. This transition appears gradual, indicating turbulent mixing in this region. On 5 June and the ascents of 6 and 7 June, the SHI and the cloud are directly coupled by turbulent mixing. For the descents of 6 and 7 June, most of the mixing takes place at the interface of the cloud top with the gap between cloud and SHI. In this case, inside the SHI the turbulence intensity is reduced almost to the free-troposphere level and the ~~virtual sensible heat flux estimate for the cloud top region is negative. This agrees with the sign of the flux estimate on the slant profile of $H \approx -3.5$ at cloud top. Because the temperature and specific humidity gradients have the same sign, the moisture flux and the measured~~ SHI seems to be decoupled from the cloud layer via the gap in between.

5.2 Vertical profiles of turbulent moisture and heat fluxes

The turbulent exchange of moisture can be quantified by the latent heat flux

$$L = \overline{\rho} \cdot \mathrm{L_v} \cdot \overline{w'q'}, \tag{4}$$

whereas the virtual sensible heat flux ~~should be orientated in the same direction. We conclude, that the negative cloud top flux on 6 June suggests entrainment of humid air from above into the cloud.~~

~~On 5 June, the missing flux estimates close to cloud top do not allow for a conclusion about entrainment. On 7 June, only a weak negative virtual heat flux of -1 is measured around 50 above~~ is given by

$$H = \overline{\rho} \cdot c_p \cdot \overline{w'\theta'_v}, \tag{5}$$

with an overline describing an average of the sub-record. Here, θ_v is the virtual potential temperature (as measured by the ultrasonic anemometer), $L_v = 2.5 \cdot 10^6\,\mathrm{J\,K^{-1}}$ is the latent heat of evaporation, and $c_p = 1005\,\mathrm{J\,kg^{-1}\,K^{-1}}$ is the specific heat capacity of air. This direct calculation of H and L requires sufficient long, stationary, and homogeneous records in a certain constant height to provide time-averaged estimates of the covariances with statistical significance (Stull, 1988; Lenschow et al., 1994). Our observations focus mainly on vertical profiling and only a very limited number of height-constant records around the cloud top ~~on the slant profile~~and inversion region is available. Therefore, ~~no statement can be made about entrainment for the measurements conducted on 5 and 7 June 2017.~~

5.2.1 ~~Gradient method fluxes~~

~~One key issue concerning the observed humidity layers above cloud top is their interaction with the cloud layer via vertical moisture transport. Due to limitations of the BELUGA instruments (e.g. the lack of a fast response humidity sensor) , only the virtual sensible heat flux H can be directly estimated~~ we apply two approaches for estimating fluxes from vertical profiles: (i) describing the flux profile by applying the ~~eddy covariance method. Based on turbulence parameters in combination with the mean profiles of q and θ_v, a rough estimate (at least of the sign) of the moisture flux is possible in order to draw conclusions about the vertical moisture transport. The q and θ_v fluxes are additionally influenced by the liquid water flux(de Roode and Duynkerke, 1997; Nicholls, 1984). Here, we neglect the effect of cloud water phase transition at cloud top and assume the q and θ_v fluxes to be independent from each other.~~

~~Based on the classical boundary layer theory (e.g. Stull, 1988), the turbulent energy fluxes are related to the vertical~~ so-called "slant profile method" and (ii) relating the turbulent flux to mean gradients (flux gradient method).

The slant profile method is based on the assumption that for a certain height range the profile data are considered as a homogeneous record and Eq. 5 can be applied. For this method, instantaneous values of H are estimated for a defined height range, defining also the length scales contributing to the flux. For our observations, this method provides only results for H due to the lack of fast-response humidity measurements. The flux gradient method is based on the relation between the covariances and the mean gradients of ~~the respective parameter x by:~~ θ_v and q:

$$\overline{w'\theta'_v} = -K_x - K_H \cdot \frac{\partial \overline{x}}{\partial z} \frac{\partial \overline{\theta}_v}{\partial z}, \tag{6}$$

~~with $K_x \geq 0$~~ and

$$\overline{w'q'} = -K_Q \cdot \frac{\partial \overline{q}}{\partial z} \tag{7}$$

with K_H and K_Q being the turbulent exchange ~~coefficient. This relationship does not consider counter-gradient fluxes, which , however, should be negligible in strong inversions.For heat and moisture, it has been shown that $K_H \approx K_Q$~~ coefficients for

sensible and latent heat, respectively. The coefficients are defined as positive, which means that the flux is directed against the mean gradient. Values of K can be derived from parameterizations based on turbulence observations such as proposed by Hanna (1968) or by directly applying Eq. 6 with the measured H, yielding K_H. With $K_\mathrm{Q} \approx K_\mathrm{H}$ (Dyer, 1967) for a wide range of stratification ~~. We cannot provide a direct estimate for K_H or K_Q to apply the gradient method. Instead, we can estimate the exchange coefficient for momentum K_m: Hanna (1968) suggested~~

~~$$K_\mathrm{m} = \mathrm{C} \cdot \frac{\sigma_\mathrm{w}^4}{\varepsilon}$$~~

~~with C = 0.35.The required basic turbulence observations σ_w and ε are available from measurements obtained with the BELUGA instrument setup.Finally~~and the mean humidity gradient $\partial\overline{q}/\partial z$, we estimate L by combining Eq. 7 and Eq. 4.

Before estimating H from the slant profiles by applying Eq. 5, the turbulent ~~Prandtl number $\mathrm{Pr_t} = K_\mathrm{m}/K_\mathrm{H}$ relates the exchange coefficients of momentum and heat. The Prandtl number is~~ fluctuations must be determined. This is done by applying a high-pass filter of Bessel type with a filter window of 10 s, corresponding to a ~~function of vertical thermodynamic stability, but ranges from 0.5 to 1 (Li, 2019). Here, we consider $\mathrm{Pr_t} \approx 0.7$ as suggested by Stull (1988), although there is a controversial discussion about $\mathrm{Pr_t}$ in particular for stable conditions such as the inversion layer (e.g. Grachev et al., 2007).~~

~~For the observations performed on 6 June 2017, we estimate from the horizontal BELUGA flight leg at cloud top $\sigma_\mathrm{w}^2 \approx 0.03\,\mathrm{m^2\,s^{-2}}$ and $\varepsilon \approx 4 \cdot 10^{-4}\,\mathrm{m^2\,s^{-3}}$, yielding $K_\mathrm{m} \approx 0.95\,\mathrm{m^2\,s^{-1}}$ and $K_\mathrm{H} = K_\mathrm{Q} \approx 1.35\,\mathrm{m^2\,s^{-1}}$. The values estimated from the slant profile are by a factor of almost five smaller yielding $K_\mathrm{H} = K_\mathrm{Q} \approx 0.28$. In the following, we use the values derived from the slant profile for convenience; a quantitative description of the wave influence is not possible at this point~~horizontal length scale of about 10 m to 70 m (depending on the horizontal wind velocity) and a vertical length scale of about 10 m. After filtering, the fluxes are averaged over a moving 50 s window by applying Eq. 5. The filter and averaging windows are similar to the values proposed by Tjernström (1993) and Lenschow et al. (1988), who estimated turbulent fluxes from aircraft-based slant profiles.

~~With a vertical temperature gradient of 0.18 (estimated for the hatched height range in~~ Figure 12 shows five selected cases (cf. Fig. ~~9a) , we calculate:~~

~~$$H = -\overline{\rho} \cdot \mathrm{c_p} \cdot K_\mathrm{H} \cdot \frac{\partial \overline{\theta}_\mathrm{v}}{\partial z}$$~~

~~and obtain $H \approx -59\,\mathrm{W\,m^{-2}}$, which is four times higher compared to the direct covariance estimate ($H = -15$). For the same height range in Fig. 9b, the vertical specific humidity gradient is estimated to 0.025 and the latent heat flux~~

~~$$L = -\overline{\rho} \cdot L_\mathrm{v} \cdot K_\mathrm{Q} \cdot \frac{\partial \overline{q}}{\partial z}$$~~

~~with the latent heat of evaporation $L_\mathrm{v} = 2.5 \cdot 10^6\,\mathrm{J\,K^{-1}}$ yields $L \approx -21$. For the case observed on 7 June, the turbulent exchange between cloud top and inversion layer is less pronounced and with $K_\mathrm{H} = K_\mathrm{Q} \approx 0.13$ we estimate $H \approx -24\,\mathrm{W\,m^{-2}}$ and $L \approx -6\,\mathrm{W\,m^{-2}}$, respectively. The fluxes are weaker because of the higher variance and dissipation rate prevailing on~~ 11) with profiles of H based on the slant profile method and L based on the flux gradient method. The upper part of the cloud

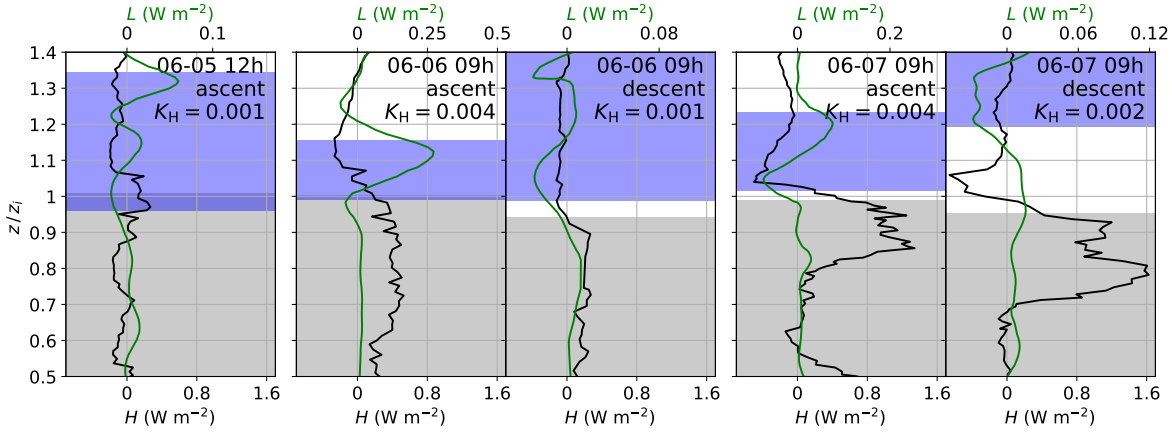

Figure 12. As Fig. 11, but for the virtual sensible heat flux H (eddy covariance method) and the latent heat flux L (flux gradient method).

layer is mainly characterized by an upward oriented heat flux ($H > 0$), most pronounced for the last two profiles with a local maximum between $0.8 < z/z_i < 1$. Only for the first ascent of 5 June, the H flux is almost height-constant with much lower values compared to the other days. For this day, θ_v exhibits larger variability around and slightly above z_i, which differs from the typical structure of a turbulent flow. This variability mainly causes the positive values of H around z_i, which, therefore, should not be misinterpreted. Such an effect is investigated in more detail in Sect. 5.1. A negative peak of H around or slightly above z_i is visible for the descent of 6 ~~June, although the~~ June and both profiles of 7 ~~June case exhibits stronger wind shear and less stability close to the cloud top. Turbulence parameters (vertical wind variance σ_w^2, dissipation rate ε and turbulent exchange coefficients K_m, K_H and K_Q) and turbulent fluxes (H and L) estimated from the gradient method on the slant profiles on 6 and 7 June 2017 6~~ June. On 7 ~~June σ_w^2 ($m^2 s^{-2}$) 10^{-2} $5 \cdot 10^{-3}$ ε ($m^2 s^{-3}$) $2 \cdot 10^{-4}$ 10^{-4} K_m ($m^2 s^{-1}$) 0.19 0.09 $K_H = K_Q$ ($m^2 s^{-1}$) 0.28 0.13 H ($W m^{-2}$) -59 -24 L ($W m^{-2}$) -21 -6 All turbulence parameters observed during the slant profile BELUGA flight tracks are summarized in Table ??. The gradient methodis not applied to the 5 June results, because there is hardly any measurement of dissipation in the inversion layer due to the resolution of the Sonic anemometer. For the measurement cases on 6~~ June, a secondary, weaker negative peak in H is located at the lower part of the SHI.

Although it is known that in general $K = K(z)$, we estimate a constant K_H for each ascent and descent in the lower region of the SHI, which is the focus area of our study. In that region, we observe negative H fluxes and positive θ_v gradients. Applying Eq. 6 leads to mean values of K_H between 0.001 $m^2 s^{-1}$ and 0.004 $m^2 s^{-1}$ for the five profiles. The $K_H (= K_Q)$ values for each profile are used for calculating the L profile based on the flux gradient method.

A negative peak in L is observed for all days in the lower SHI region. The downward energy flux at cloud top is common for the entrainment region, where potential warmer and usually drier air from the free troposphere is mixed downward into the (cloudy) ABL. However, for our observations, this downward flux in the lower SHI region means a downward transport of potential warmer but more humid air into the region below. The situation is different for the descent profile of 7 ~~June,~~

the observations consistently show negative latent and virtual sensible heat fluxes at cloud top , meaning a downward flux of sensible and latent heat from the humidity layer into the June, with the vertical gap between cloud top and SHI. Here, the negative peak in L at the lower SHI is accompanied by a positive L at cloud top. This negative sign is a direct consequence of the positive gradients of potential temperature and moisture above profile does not suggest a significant transport of humidity into the cloud top. Instead, for the special case where the cloud and the SHI are separated, the gap in between receives moisture from both the SHI above and from the cloud layer below.

6 Large Eddy Simulations (LES)

To further investigate the turbulent transport processes between the SHI and the cloud top, the in situ measurements are complemented with LES. The LES provides the turbulent flux of humidity in the vicinity of the inversion, which gives information about the interaction of the humidity layer with the underlying mixed layer.

5.1 Model configuration

The LES configuration adopted in this study was designed by Neggers et al. (2019) for the PASCAL observation period 5–7 June 2017. The Dutch Atmospheric Large-Eddy Simulation model (DALES, Heus et al., 2010) is applied and equipped with a well-established double moment mixed-phase microphysics scheme (Seifert and Beheng, 2006). A Lagrangian framework is adopted following evolving cloudy mixed layers in warm air masses as they moved towards the RV *Polarstern*.The simulated doubly periodic domains are discretized at 10 vertical and 20 horizontal resolution, while the large-scale forcing is derived from analysis and forecast data of the European Centre for Medium-range Weather Forecasts (ECMWF). Surface temperature is prescribed, while the surface fluxes are interactive, resulting in weakly coupled cloudy mixed layers. The temperature inversion height z_i and cloud layer boundaries are free to evolve.The simulations are constrained by in situ radiosonde profiles and evaluated against further independent cloud measurements. Eight cases are constructed during the three-day study period, capturing the variation in cloud and thermodynamic properties observed during this period.

The PASCAL simulations described above are thoroughly evaluated against measurements. Although in general the LES reproduces these to a satisfactory degree and also does produce humidity inversions, their strength and depth is underestimated. For this reason additional simulations are performed for this study, designed to better represent the observed humidity layers on

5.1 Observations at constant altitude in the inversion layer

To get a deeper insight into the transition from cloud top to the humidity layer above, measurements were taken at a constant height in this region. Figure 13 shows a 500 s time series measured on 6 June at a constant altitude around $z_i \approx 300$ m (second last constant altitude segment in Fig. 2 for 6 and 7 June 2017. The configuration of these new simulations differs from the setup described above in three aspects: Instead of starting two days in advance, the model initializes only 12 hours before the arrival of the Lagrangian air parcel at RV *Polarstern*. A shorter lead time allows to adjust the initial conditions such that a good

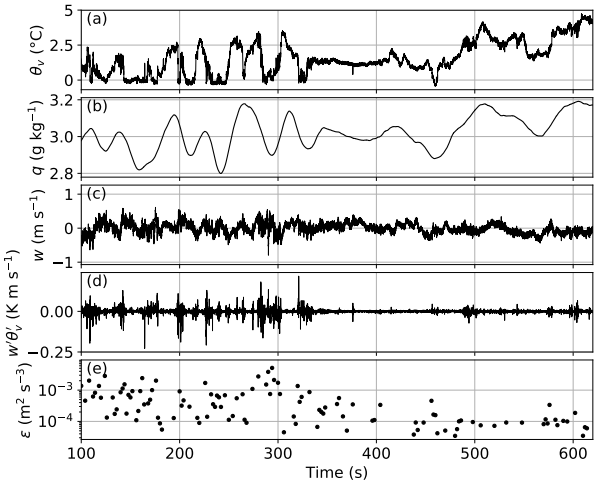

Figure 13. Constant-altitude time series of (a) virtual potential temperature θ_v, (b) specific humidity q, (c) vertical wind w, (d) co-variance $\theta_v{}'w'$, and (e) dissipation rate ε for 6 June measured at 300 m altitude around z_i.

~~agreement is obtained with the BELUGA sounding in terms of temperature inversion height. On the other hand, a period of 12 hours is still long enough to allow complete spin-up of the mixed-phase clouds. The initial state adjustments include a lowering of the inversion height, following the method of Neggers et al. (2019). However, in addition a humidity layer of 200~~June).

Within the first third of the record, θ_v shows strong variations on a typical time scale of 30–50 s with amplitudes up to 3 K. Based on the temperature gradient (Fig. 9), the changes in θ_v would correspond to a height variation of ~ 10 m. More likely, parts of the height-constant measurements ($\Delta z \approx 1$ m~~depth and 0.5 strength is superimposed on the initial profile, placed immediately above~~) are taken in potential colder, drier, and more turbulent air masses at the inversion base, interrupted by measurements in potential warmer, more humid, less turbulent air masses at higher altitudes well within the T inversion. This variability is also visible in the wind direction (not shown here). Depending on the relative location of z_i to the ~~new temperature inversion . These values reflect the structure of~~ measurement height, the co-variance $w'\theta_v'$ is highly intermittent and no mean flux is derived from these observations.

The center part of the record is characterized by a comparable low variability leading to the conclusion that this part of the observations is performed at an almost constant distance to z_i. Finally, observations are performed well above z_i inside the stably stratified T inversion layer, characterized by values of ε one order of magnitude lower compared to at the inversion base. Here, variations in θ_v and q are again correlated and caused by changes in relative height.

The observations do not allow for drawing quantitative conclusions, such as time and area-averaged turbulent heat fluxes, from this record. However, these measurements vividly illustrate the difficulties in estimating turbulent fluxes based on covariance methods in the vicinity of the temperature inversion, although the measurement height is kept at a remarkable constant height level.

6 Possible influence of the humidity layer on ABL and cloud structure: A preliminary LES case study

We provided new observational insights into the turbulent structure of the ~~observed SHIs. The surface sensible and latent heat fluxesare switched off, in effect decoupling the cloud layer from the surface. Imposing a surface decoupling has proven to be an effective way to maintain humidity inversions (Solomon et al., 2014). It should be noted that no measurements were made of the surface heat fluxes along the upstream trajectory, preventing us from assessing the validity of this modification. These modifications make the case slightly idealized, but are justified by our goal of working with an LES realization in which the strength and depth of the humidity layersmore or less matches the BELUGA observations. This is prerequisite for using LES data alongside BELUGA data for studying humidity inversion processes such as turbulent fluxes. For reference, the simulations are repeated for an initial state without the SHI superimposed. Because the method described above works best for the 7 June case, the results for this day are discussed below. The 6 June case is briefly touched, but the results exhibit some numerical artefacts, which are outlined~~ cloudy ABL capped by humidity layers. However, for understanding how these observed humidity layers influence the general ABL and cloud development, numerical studies such as large-eddy simulations (LES) are necessary. The LES described in this section provide first indications for the effects of the SHI on the dynamics of a cloudy ABL.

The LES configuration was designed by Neggers et al. (2019) for the PASCAL observation period 5–7 June 2017. A Lagrangian framework is adopted following evolving cloudy mixed layers as they move towards the RV *Polarstern*. The original model setup is slightly modified for the present study. Further information about the model configuration can be found in Appendix ~~??~~.

6.1 ~~Comparison of LES and BELUGA results~~

~~Comparison of LES results (with and without an initial SHI) and BELUGA observations for 7 June 2017: Vertical profiles of (a) virtual potential temperature θ_v, (b) specific humidity q, (c) liquid (LWC) and ice water content (IWC) of the LES, (d) virtual sensible heat flux H and (e) latent heat flux L. The light blue area is the cloud extent for the observations (cloud top is derived as in Sect. 2 for BELUGA, cloud base is from Cloudnet). Figure 14 shows vertical profiles of the LES output and of BELUGA measurements (Fig. 10) for~~ A. Here, we provide a selected case study of 7 ~~June 2017.~~ June 2017, for which the simulations reproduce the observed humidity layers. The LES profiles ~~are results of the 12 simulations ,~~ result from the simulations ending at the location of RV *Polarstern* at 10:48 UTC. ~~Here, all~~ All variables represent horizontal averages over the full LES domain (2.56~~ km~~ × 2.56~~ km~~) and are averaged over 900~~ s~~. This includes the turbulent fluxes of heat H and moisture L, calculated as the covariance between vertical velocity and perturbations in static energy and humidity, respectively. ~~The LES results are shown for simulations with~~ For reference, the simulations are repeated with an initial state without the SHI superimposed.

Figure 14 shows vertical profiles of the LES output (with and without an initial SHI~~.~~) and the BELUGA ascent, where cloud top, z_i and SHI base coincide. The temperature difference across the inversion as well as temperature gradients are comparable for the LES and the observations (Fig. 14a). With an initial SHI in the LES, the temperature inversion base z_i, and therefore the mixed layer height, agrees well with the observed ~~inversion base (Fig. 14a).~~

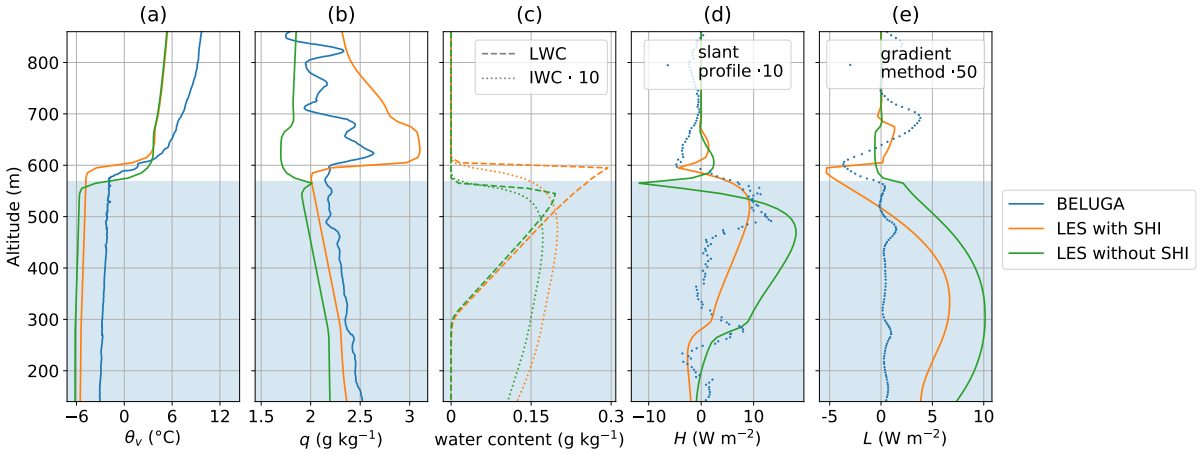

Figure 14. LES results (with and without an initial SHI) and BELUGA observations for 7 June 2017: Vertical profiles of (a) virtual potential temperature θ_v, (b) specific humidity q, (c) liquid (LWC) and ice water content (IWC), (d) virtual sensible heat flux H and (e) latent heat flux L. The light blue area is the cloud extent for the observations (cloud top is derived from BELUGA irradiance measurements, cloud base from lidar data).

z_i. Without the initial humidity layer, ~~the temperature inversion base~~ z_i is around 40 m lower. ~~A constant temperature offset of around 2 between measured and simulated profiles is present, which is due to the initial LES profile based on a radiosounding. The temperature difference across the inversion as well as temperature gradients are comparable. The~~ The vertical profile of specific humidity shows a similar vertical structure and a distinct increase of q above the cloud layer in both the model and the observations (Fig. 14b). The strength of the SHI of Δq = 1.1 g kg^{-1} in the LES is close to the observed humidity inversion strength of Δq = ~~0.7~~ 0.6 g kg^{-1}. In the LES without initial SHI, specific humidity decreases by $\Delta q \approx 0.2$ g kg^{-1} within the temperature inversion height range.

Compared to the balloon measurements, a thinner liquid cloud layer forms in the LES, as indicated in the LWC profiles in Fig. 14c. While the observed ~~cloud was around 400~~ mixed-phase cloud is around 500 m thick, the simulations result in a liquid cloud of about 300 m vertical extent. Note that significant ice water is present below the liquid cloud base in the model, for which ~~ceilometer~~ lidar readings are sensitive (Bühl et al., 2013). For this reason, the model bias in cloud base height could be artificial. Without a humidity layer, the liquid cloud is ~~slightly~~ thinner, extending only 260 m. The cloud top is simulated at around 600 m altitude for the scenario with SHI and at 560 m altitude for the scenario without SHI, respectively. ~~In both cases, the cloud top is slightly (10–20) above the temperature inversion base. In the~~ In the SHI case, the higher cloud top reflects the larger mixed layer depth compared to the case without SHI.

The ~~BELUGA measurements performed on 7 June provide sensible heat flux measurements on the slant profile, which means that flux magnitude is underestimated and allowing only a qualitative comparison to the LES . Both BELUGA and LES provide a positive~~ LES provides a positive (i.e. upward-directed) virtual sensible heat flux inside the cloud layer ~~, increasing~~

with altitude (Fig. 14d). In the LES, a noteworthy feature is the The negative virtual heat flux at cloud top , which is seen with and without initial SHI(-5 and -12 , respectively). In the BELUGA observations, a small negative virtual sensible heat flux of -1 is present around 50 above cloud top. Unfortunately, the BELUGA instrumentation does not provide moisture flux measurements. . The LES, with or without an initial SHI, shows a positive (i.e. upward directed) moisture flux L between surface and cloud top with a maximum at cloud base (Fig. 14e). In the presence of an initial SHI, the cloud top region exhibits a negative moisture fluxof -5 . . This negative moisture flux coincidences coincides with the negative virtual sensible heat flux , and indicates that downward humidity transport takes place between the humidity layer and the underlying mixed layer. Lacking the initial SHI, the total moisture flux is close to zero near the inversion. This means that in this case dry air, rather than humidity, is entrained into the mixed layer from above. In Sect. 5 we argue that the cloud top virtual sensible heat flux might be an indicator for the direction of the moisture flux. This The direction of fluxes is in agreement with the LES results for 7 June with an SHI, where both fluxes point into the same direction, whereas the LES without SHI shows a negligible moisture flux .

For the 6 June simulations (Fig. **??**), the LES with SHI matches the observations well in terms of temperature inversion height, but the vertical profile of q is not as well represented as flux estimates in Sect. 5.2 for 7 June. The impact of removing the initial SHI is the same as for 7 June: The temperature inversion stays around 40 lower, and the liquid cloud layer remains thinner (230 thick compared to 300 thick with initial SHI). At cloud top, a negative H is visible with and without SHI (-11 and -10 , respectively). With SHI, at cloud top a weak negative L of -0.3 is present , whereas without SHI there is no significant negative peak at cloud top. Although for L the simulations show some numerical artifacts inside the SHI (as explained in Appendix **??**), the main conclusion for the 6 June case is the same as for 7 June: The humidity layer provides moisture for the cloud, manifested by a downward moisture flux at cloud top.

7 Discussion

6.1 Formation of specific humidity inversions

Before exploring the interactions of the SHIs with clouds, we briefly discuss their origin. Mostly, the formation of Arctic summertime SHIs is attributed to large-scale advection of humid air masses (Solomon et al., 2014; Naakka et al., 2018). Tjernström et al. (2
developed a conceptual model for air mass transformation during moist and warm air advection over open water and sea ice: When warm, humid air is advected over sea ice, the air mass is cooled by the surface, a surface temperature inversion develops and fog or low clouds form. Cloud top buoyancy and surface roughness enhance mixing, the mixed layer deepens and the clouds lift from the surface. The last stage is the well-mixed, cloud-capped, persistent ABL, which has been observed frequently in the Arctic. During the air mass transformation, the cooling within the ABL results in condensation and subsequent precipitation, which reduces the specific humidity. Specific humidity above the ABL is not affected and, as a result, an SHI at the top of the ABL forms. where a SHI is present above cloud top on the ascent.

Five-day back trajectories ending at RV *Polarstern* (gray dot) at 00:00 and 12:00 UTC between 5 and 7 June 2017 in altitudes 50m (red), 250m (blue) and 1000m (green). The trajectories are calculated using HYSPLIT (Stein et al., 2015)

. The LES trajectories for 6 and 7 June (on the 950 isobar) are added as black lines. Sea ice data are for 6 June 2017 (Maslanik and Stroeve, 1999).

Figure **??** shows back trajectories of the air masses for the study period between 50 and 1000 altitude. The trajectories are calculated using the Hybrid Single-Particle Lagrangian Integrated Trajectory model (HYSPLIT; Stein et al., 2015). The air mass during the study period originates further south in the Arctic ocean and is advected over open water and sea ice. Towards the end of the period, the air mass resides locally over the sea ice after being advected, which is also seen in the change in wind direction (Fig. 7d). The HYSPLIT trajectories compare well with the 12-hour trajectories used for the Lagrangian LES study, which are based on analysis and forecast data of the Integrated Forecast System (IFS) of the ECMWF model.

If the conceptual model of Tjernström et al. (2019) is applied to the air mass history in the study period, the state at RV *Polarstern* corresponds to the final state with an elevated temperature inversion above the mixed layer and a cloud deck. The formation of the humidity layer is probably a result of warm air advection over sea ice. It remains open why the observations do not only show an SHI, but instead a well-defined layer of increased humidity above the cloud. One reason might be vertically differential advection.

6.1 Cloud top fluxes

The virtual sensible heat flux at cloud top is estimated with the direct eddy covariance method on constant altitude legs and on the slant profile. This is complemented by applying the gradient method to the observations in order to add the latent heat flux. For both methods, the fluxes on the slant profile are somewhat smaller than on the constant altitude legs (for the 6 June case a factor of four to five). There are two possible explanations for this difference: (i) the values derived from the horizontal legs are more reliable and statistically more robust because more eddies of the typical integral length scale $\mathcal{L} \propto \sigma^3/\varepsilon \approx$ 6–15 (Wyngaard, 2010) have been sampled, and (ii) gravity waves (see discussion in Sect. **??**) may also influence the estimates of the variance and dissipation and, therefore, the turbulent exchange coefficients.

The fluxes based on the observations on 6 and 7 June can be compared to the LES fluxes. The cloud top flux magnitudes from the gradient method (Table **??**) differ from the LES fluxes (Fig. 14 and Fig. **??**) by a factor of up to five for the most part. For 6 June, the LES cloud top virtual heat flux of -11 is close to the direct observational estimate of -15 . In summary, all cloud top fluxes (from both observational flux methods and the LES) on 6 and 7 June are consistently negative. Further, the LES provides K_H from the LES fluxes and the vertical temperature gradient by applying Eq. (**??**). The values for the LES ($K_\mathrm{H} \approx 0.03$ for 6 June and $K_\mathrm{H} \approx 0.02$ for 7 June) are one order of magnitude lower than the observed values of 0.28 and 0.13 .

However, a day-to-day comparison and a comparison between LES and observations should not be over-interpreted. Applying both observational flux methods on one single profile results in an instantaneous flux estimate compared to area- and time-averaged fluxes as done for the LES. Further, the observed fluxes on constant altitude legs are averaged over a limited time period. From a statistical point of view, the three methods provide comparable results only if the integral time scales τ are small compared to the sampling time T_s. The relative error of the flux measurement due to the random nature of the temperature and vertical

velocity field is given by:

T_s.

765

(Lumley and Panofsky, 1964). For the slant profile method on 6 June, we integrate the measurements over $T_s = 50$ and estimate an integral time scale $\tau = \frac{\mathcal{L}}{U} = \frac{6\,\mathrm{m}}{5\,\mathrm{m\,s^{-1}}} = 1.1$, yielding a relative error of $\Delta H \approx 20\%$. For the leg at constant height ($\tau = \frac{15\,\mathrm{m}}{5\,\mathrm{m\,s^{-1}}} = 3$), a 10 long sample was taken reducing ΔH to $\sim 10\%$. Note that this is only the random sampling error ignoring the possible influence of sensor noise, the influence of gravity waves or violations of a homogeneous and stationary sample.

770 This approach does not allow to directly compare the results for the eddy covariance method, the gradient method and the LES. Instead, it shows that an instantaneous measurement can deviate significantly from averaged samples. Nevertheless, the main ABL feature results from all methods: consistent negative fluxes of virtual sensitive heat and latent heat at cloud top, indicating entraiment of humid air into the cloud.

6.1 Influence of the humidity layer on cloud lifetime

775 The LES study by Neggers et al. (2019) investigates remote and local controls on the mixed layer evolution. Amongst others, it is concluded that gradual and continuous entrainment deepening of the mixed layer (a local process) is observed as long as a cloud is present. Near the temperature inversion, large-scale vertical advection (subsidence and upsidence) is the main control of deepening or shallowing.

Strong sudden subsidence events may cause cloud collapse with a rapid decrease in mixed layer depth. The Cloudnet 780 observations show that the cloud layer on 6 June shallows and descends (Fig. 1), but does not decay although subsidence is present. While the SHI strength is generally underestimated in the original LES, the larger observed SHI strengths may be responsible for maintaining the mixed layer thickness by supplying enough moisture for entrainment processes to prevent cloud collapse.

This is supported by the 12 trajectories used for the LES presented in Sect. 6, which exhibit a thinner cloud layer when 785 no initial SHI is present. Further, the simulations show that the SHI is responsible for an elevated mixed layer height. Less terrestrial radiative cooling due to a reduced cloud top LWC implies a lower entrainment rate, so that the inversion rises less quickly. The fact that this impact is the same for the 6 and 7 June case, although the cases are different (6 June with subsidence, while 7 June exhibits upsidence), makes this a robust result.

More research is necessary to further investigate how the additional entrained moisture of the humidity layer is processed in 790 the cloud (e.g., through phase transition) and how exactly the humidity layer contributes to the cloud evolution (e.g., the role of clouds penetrating into the inversion or thermodynamically decoupled clouds).

In this study, layers

7 Summary and conclusion

A persistent layer of increased specific humidity ~~(so-called specific humidity inversions, SHI) above Arctic stratocumulus and their interactions with the underlying cloud layer are investigated by means of tethered balloon-borne observations in the~~ above a stratocumulus deck has been observed by tethered-balloon borne instrumentation in the Fram Strait north-west of Svalbard (82° N, 10° E) ~~. A persistent layer of increased specific humidity above the stratocumulus deck is observed and analyzed in detail over a three-day~~ in the period from 5 to 7 June 2017. ~~The observational data is supplemented with results from dedicated LES experiments that are based on field campaign data.~~

~~Local ABL parameters(temperature, humidity, wind~~ Vertical profiles of thermodynamic parameters, ~~terrestrial irradiance and eddy dissipation) are sampled by~~ wind velocity, and terrestrial irradiance were sampled in situ~~measurements with high-resolution instruments for collocated turbulence and radiation observations. Typically, the sampling strategy of the balloon observations is based on continuous vertical profiling combined with short (≈ 10 min) flight legs at constant height allowing for statistically significant sampling of turbulence parameters. It turns out to be challenging to position the balloon for a longer time inside a shallow temperature inversion layer above cloud top to sample under homogeneous and stationary conditions. This is partly caused by the usually non-stationary~~ . The high resolution of the measurements allows for estimating local turbulence parameters such as local energy dissipation rates. Based on slant profiles, the turbulent virtual sensible heat flux was estimated by applying the eddy covariance method. The vertical profile of the latent heat flux was calculated by applying the flux gradient method. The observations allow for the first time detailed analyses of the relative position of the SHI, cloud top and the temperature inversion height z_i and give a first qualitative indication of how these different layers are coupled by turbulent transport.

Two different scenarios have been observed: (i) the base of the SHI qualitatively coincides with z_i and the cloud top height and ~~the varying height of the balloon itself (although this is a minor issue for this study), which causes significant uncertainties in a region with strong gradients. Furthermore, non-turbulent features such as gravity waves in the temperature inversion violate classical Reynolds decomposition, resulting in further uncertainties of the estimated turbulent fluxes~~ (ii) cloud top height and z_i had decreased with the SHI base remaining at a constant height, leading to a "humidity gap" between cloud top and SHI base. Turbulence, as described by local ε, decreased gradually above z_i suggesting that turbulent energy exchange is possible in that region. Vertical profiles of latent heat fluxes qualitatively show a downward moisture transport at the base of the SHIs for all profiles. When the SHI coincides with the cloud top as for the first scenario (i), this suggests the cloud being supplied with moisture from the overlying SHI. For the second scenario (ii), the sign of the latent heat fluxes suggests upward humidity transport from the cloud together with downward humidity transport from the SHI base, both feeding the vertical gap between the SHI base and the cloud top with moisture.

~~Although partly limited due to specific measurement conditions, direct turbulent flux measurements in the temperature and humidity inversion layer are presented and compared with gradient method estimates. For the measurement case observed on 6 June 2017, direct flux estimates at cloud top yield a negative virtual sensible heat flux, which indicates downward entrainment of humid air from above into the cloud layer. The absolute value of the fluxes remains uncertain due to the possible influence~~

~~of gravity waves and necessary filtering, but – together with gradient flux estimates and LES – a negative latent heat flux of -5 to -20 is derived. We conclude that the increased humidity above the cloud provides the necessary moisture to sustain the cloud layer in the observed case~~For one case study of the first type scenario, LES were performed.

~~LES are performedto complement the observations on 6 and 7 June.~~ The simulations ~~confirm the negative virtual sensitive heat fluxes and moisture fluxes at cloud top. Simulations without an initial SHI do not show the downward moisture flux at cloud top~~support the observational findings by showing a negative moisture flux at the SHI base towards the cloud region below. Further, ~~analyses of the LES reveal that the SHI is responsible for a slightly thicker cloud layer than in cases without SHI. In addition,~~ the ~~presence of a humidity layer causes an elevated inversion base and cloud layer, which might contribute to sustain the cloud.~~ LES show that the moisture supply does directly influence the dynamics of the cloudy ABL by increasing z_i and the cloud layer thickness.

For more general conclusions beyond case studies, further observations over a larger measurement period are necessary. An improvement for future measurements would be a fast-response humidity sensor that operates reliably under cold and cloudy conditions. Those observations would allow for quantifying the vertical moisture transport by applying the eddy covariance method instead of relying on estimating the exchange coefficient and mean humidity gradients.

Furthermore, we suggest a thorough LES study driven by our observations. These studies are capable of investigating the consequences of the two observed scenarios on ABL dynamics and cloud life-time and will help to answer the question of how important the SHIs are for the Arctic cloudy ABL.

~~The new BELUGA tethered balloon system proved its unique capabilities to examine the turbulent structure of cloud-topped Arctic boundary layers. These observations motivate further detailed investigations of SHIs and their influence on cloud layers. Improvements of the instrumentation, such as including fast humidity sensors and cloud microphysical observations, will allow for a more detailed insight into the cloud top processes. It is not yet clear how exactly the additional moisture above cloud top influences the cloud development and lifetime. This question can be answered by future extended observations in combination with more detailed model studies.~~

Appendix A: LES ~~for 6 June 2017~~model configuration

~~Figure ?? shows LES results for the 6 June 2017 case. While the LES successfully reproduces an SHI, it is less pronounced as in the~~ The LES configuration adopted in this study was designed by Neggers et al. (2019) for the PASCAL observation period 5–7 June 2017. The Dutch Atmospheric Large-Eddy Simulation model (DALES, Heus et al., 2010) is applied and equipped with a well-established double moment mixed-phase microphysics scheme (Seifert and Beheng, 2006). A Lagrangian framework is adopted following evolving cloudy mixed layers in warm air masses as they moved towards the RV *Polarstern*. The simulated doubly periodic domains are discretized at 10 m vertical and 20 m horizontal resolution, while the large-scale forcing is derived from analysis and forecast data of the European Centre for Medium-range Weather Forecasts (ECMWF). Surface temperature is prescribed, while the surface fluxes are interactive, resulting in weakly coupled cloudy mixed layers. The temperature inversion height z_i and cloud layer boundaries are free to evolve. The simulations are constrained by in situ radiosonde profiles and

evaluated against further independent cloud measurements. Eight cases are constructed during the three-day study period, capturing the variation in cloud and thermodynamic properties observed during this period.

The PASCAL simulations are thoroughly evaluated against measurements. Although in general, the LES reproduces these to a satisfactory degree and also does produce humidity inversions, their strength and depth are underestimated. For this reason, additional simulations are performed for this study, designed to better represent the observed humidity layer on 7 ~~June case (see Fig. 14). Perhaps this is due to the SHI being much shallower on this day; as a result, it is resolved less well in the LES, and probably overly weakened by subgrid diffusion. A few features in the L profile capture the eye that are probably related:~~ June 2017. The configuration of these new simulations differs from the setup described above in three aspects:

- Instead of starting two days in advance, the model initializes only 12 hours before the arrival of the Lagrangian air parcel at RV *Polarstern*. A shorter lead time allows adjusting the initial conditions such that a good agreement is obtained with the BELUGA sounding in terms of temperature inversion height. On the other hand, a period of 12 hours is still long enough to allow complete spin-up of the mixed-phase clouds.

- The ~~simulation including an SHI (orange) shows a positive peak in L in the middle of the humidity layer~~ initial state adjustments include a lowering of the inversion height, following the method of Neggers et al. (2019). ~~This peak suggests that weak turbulent overturning takes place inside that layer. Indeed, inFig. **??**(a) the simulated SHI looks too internally well-mixed, and lacks the shallow but strong peak as observed .~~

- ~~The simulation without an SHI (green line) has a pronounced negative peak in L above the LES inversion, although not at the inversion. This dip collocates with a dip in the q profile (panel b). Both features are also present in the 7 June case but much less pronounced. The dip in the flux above the thermal inversion is a well known shortcoming of centered difference advection schemes (e.g. Stevens et al., 2001), and its presence here immediately suggests that this is a numerical artefact. It is probably aggravated by the thinness of the SHI in this case, making it less resolved and thus more sensitive to the choice of the advection scheme. The enhanced internal overturning in the simulated SHI is very likely also related to this issue.~~ However, ~~note that the impact of the SHI on the cloud layer is still consistent with the 7 June case, elevating the temperature inversion and enhancing liquid cloud mass. For this reason we conclude that this numerical artefact does not significantly harm the main conclusions of this study, namely that the humidity layer acts as a moisture source for the clouds below. We will further investigate this numerical problem in the future, by applying higher vertical resolutions and testing different advection schemes in the LES~~in addition a humidity layer of 200 m depth and 0.5 $\mathrm{g\,kg^{-1}}$ strength is superimposed on the initial profile, placed immediately above the new temperature inversion. These values reflect the structure of the observed SHIs.

- The surface sensible and latent heat fluxes are switched off, in effect decoupling the cloud layer from the surface. Imposing a surface decoupling has proven to be an effective way to maintain humidity inversions (Solomon et al., 2014). It should be noted that no measurements were made of the surface heat fluxes along the upstream trajectory, preventing us from assessing the validity of this modification.

These modifications make the case slightly idealized, but are justified by our goal of working with an LES realization in which the strength and depth of the humidity layers more or less match the BELUGA observations. This is a prerequisite for using LES data alongside BELUGA data for studying humidity inversion processes such as turbulent fluxes.

~~Same as Fig. 14, but for 6 June 2017. The blue dots in panel (d) represent the eddy covariance flux estimate on constant altitude legs for BELUGA.~~

Data availability. Data related to the present article are available open access through PANGAEA – Data Publisher for Earth & Environmental Science: https://doi.pangaea.de/10.1594/PANGAEA.899803 (Egerer et al., 2019) . The LES results used in this study are available at https://doi.pangaea.de/10.1594/PANGAEA.919945 and https://doi.pangaea.de/10.1594/PANGAEA.919946.

Author contributions. UE and MG performed the measurements and analyzed the observational data. HS was responsible for the overall balloon system. HS, MW and AE contributed to the data analysis. RN performed the LES and analyzed the results. HG provided the remote sensing data and advice on the data. UE drafted the paper with contributions from all co-authors.

Competing interests. The authors declare that they have no conflict of interest.

Acknowledgements. We gratefully acknowledge the funding by the Deutsche Forschungsgemeinschaft (DFG, German Research Foundation) - project number 268020496 - TRR 172, within the Transregional Collaborative Research Center "ArctiC Amplification: Climate Relevant Atmospheric and SurfaCe Processes, and Feedback Mechanisms (AC)^3" in sub-project A02. We greatly appreciate the participation in RV *Polarstern* cruise PS 106.1 (expedition grant number AWI-PS106-00). We thank ECMWF for providing access to the large-scale model analyses and forecasts fields used to force the LES. We gratefully acknowledge the Regional Computing Centre of the University of Cologne (RRZK) for granting us access to the CHEOPS cluster. The Gauss Centre for Supercomputing e.V. (www.gauss-centre.eu) is acknowledged for providing computing time on the GCS Supercomputer JUWELS at the Jülich Supercomputing Centre (JSC) under project no. HKU28. The authors gratefully acknowledge the NOAA Air Resources Laboratory (ARL) for the provision of the HYSPLIT transport and dispersion model used in this publication.

References

Albrecht, B. A., Penc, R. S., and Schubert, W. H.: An Observational Study of Cloud-Topped Mixed Layers, J. Atmos. Sci., 42, 800–822, https://doi.org/10.1175/1520-0469(1985)042<0800:AOSOCT>2.0.CO;2, 1985.

Brooks, I. M., Tjernström, M., Persson, P. O. G., Shupe, M. D., Atkinson, R. A., Canut, G., Birch, C. E., Mauritsen, T., Sedlar, J., and Brooks, B. J.: The Turbulent Structure of the Arctic Summer Boundary Layer During The Arctic Summer Cloud-Ocean Study, Journal of Geophysical Research: Atmospheres, 122, 9685–9704, https://doi.org/https://doi.org/10.1002/2017JD027234, 2017.

Brunke, M. A., Stegall, S. T., and Zeng, X.: A climatology of tropospheric humidity inversions in five reanalyses, Atmos. Res., 153, 165 – 187, https://doi.org/https://doi.org/10.1016/j.atmosres.2014.08.005, 2015.

Bruun, H. H.: Hot-Wire Anemometry, Oxford University Press, Oxford, U.K., 1995.

Bühl, J., Ansmann, A., Seifert, P., Baars, H., and Engelmann, R.: Toward a quantitative characterization of heterogeneous ice formation with lidar/radar: Comparison of CALIPSO/CloudSat with ground-based observations, Geophys. Res. Lett., 40, 4404–4408, https://doi.org/10.1002/grl.50792, 2013.

de Roode, S. R. and Duynkerke, P. G.: Observed Lagrangian Transition of Stratocumulus into Cumulus during ASTEX: Mean State and Turbulence Structure, J. Atmos. Sci., 54, 2157–2173, https://doi.org/10.1175/1520-0469(1997)054<2157:OLTOSI>2.0.CO;2, 1997.

Deardorff, J. W., Willis, G. E., and Lilly, D. K.: Laboratory investigation of non-steady penetrative convection, J. Fluid Mech., 35, 7–31, https://doi.org/10.1017/S0022112069000942, 1969.

Devasthale, A., Sedlar, J., and Tjernström, M.: Characteristics of water-vapour inversions observed over the Arctic by Atmospheric Infrared Sounder (AIRS) and radiosondes, Atmos. Chem. Phys., 11, 9813–9823, https://doi.org/10.5194/acp-11-9813-2011, 2011.

Dirksen, R. J., Sommer, M., Immler, F. J., Hurst, D. F., Kivi, R., and Vömel, H.: Reference quality upper-air measurements: GRUAN data processing for the Vaisala RS92 radiosonde, Atmos. Meas. Tech., 7, 4463–4490, https://doi.org/10.5194/amt-7-4463-2014, 2014.

Driedonks, A. G. M. and Tennekes, H.: Entrainment effects in the well-mixed atmospheric boundary layer, Bound.-Lay. Meteorol., 30, 75–105, https://doi.org/10.1007/BF00121950, 1984.

Dyer, A. J.: The turbulent transport of heat and water vapour in an unstable atmosphere, Q. J. Roy. Meteor. Soc., 93, 501–508, https://doi.org/10.1002/qj.49709339809, 1967.

Edwards, D., Anderson, G., Oakley, T., and Gault, P.: Met Office Intercomparison of Vaisala RS92 and RS41 Radiosondes, http://go.vaisala.com/gen4/downloads/Met_Office_Intercomparison_of_Vaisala_RS41_and_RS92_Radiosondes.pdf, 2014.

Egerer, U., Gottschalk, M., Siebert, H., Ehrlich, A., and Wendisch, M.: The new BELUGA setup for collocated turbulence and radiation measurements using a tethered balloon: first applications in the cloudy Arctic boundary layer, Atmos. Meas. Tech., 12, 4019–4038, https://doi.org/10.5194/amt-12-4019-2019, 2019.

Egerer, U., Gottschalk, M., Siebert, H., Wendisch, M., and Ehrlich, A.: Tethered balloon-borne measurements of turbulence and radiation during the Arctic field campaign PASCAL in June 2017, https://doi.org/10.1594/PANGAEA.899803, supplement to: Egerer, Ulrike; Gottschalk, Matthias; Siebert, Holger; Ehrlich, André; Wendisch, Manfred (2019): The new BELUGA setup for collocated turbulence and radiation measurements using a tethered balloon: first applications in the cloudy Arctic boundary layer. Atmospheric Measurement Techniques, 12(7), 4019-4038, https://doi.org/10.5194/amt-12-4019-2019, 2019.

Grachev, A. A., Andreas, E. L., Fairall, C. W., Guest, P. S., and Persson, P. O. G.: On the turbulent Prandtl number in the stable atmospheric boundary layer, Bound.-Lay. Meteor., 125, 329–341, https://doi.org/DOI 10.1007/s10546-007-9192-7, 2007.

Griesche, H., Seifert, P., Engelmann, R., Radenz, M., and Bühl, J.: Cloudnet target categorization during PS106, https://doi.org/10.1594/PANGAEA.919344, 2020a.

Griesche, H., Seifert, P., Engelmann, R., Radenz, M., and Bühl, J.: OCEANET-ATMOSPHERE low level stratus clouds during PS106, https://doi.org/10.1594/PANGAEA.920246, 2020b.

Griesche, H., Seifert, P., Engelmann, R., Radenz, M., and Bühl, J.: OCEANET-ATMOSPHERE Cloud radar Mira-35 during PS106, https://doi.org/10.1594/PANGAEA.919556, 2020c.

Griesche, H. J., Seifert, P., Ansmann, A., Baars, H., Barrientos Velasco, C., Bühl, J., Engelmann, R., Radenz, M., Zhenping, Y., and Macke, A.: Application of the shipborne remote sensing supersite OCEANET for profiling of Arctic aerosols and clouds during *Polarstern* cruise PS106, Atmos. Meas. Tech., 13, 5335–5358, https://doi.org/10.5194/amt-13-5335-2020, 2020.

Hanna, S. R.: A Method of Estimating Vertical Eddy Transport in the Planetary Boundary Layer Using Characteristics of the Vertical Velocity Spectrum, J. Atmos. Sci., 25, 1026–1033, https://doi.org/10.1175/1520-0469(1968)025<1026:AMOEVE>2.0.CO;2, 1968.

Heus, T., Heerwaarden, C. C., Jonker, H. J. J., Siebesma, A. P., Axelsen, S., van den Dries, K., Geoffroy, O., Moene, A. F., Pino, D., de Roode, S. R., and Vilà-Guerau de Arellano, J.: Formulation of the Dutch Atmospheric Large-Eddy Simulation (DALES) and overview of its applications, Geosci. Model. Dev., 3, 415–444, https://doi.org/10.5194/gmd-3-415-2010, 2010.

Intrieri, J. M., Fairall, C. W., Shupe, M. D., Persson, P. O. G., Andreas, E. L., Guest, P. S., and Moritz, R. E.: An annual cycle of Arctic surface cloud forcing at SHEBA, J. Geophys. Res.-Oceans, 107, SHE 13–1–SHE 13–14, https://doi.org/10.1029/2000JC000439, 2002.

Jensen, M. P., Holdridge, D. J., Survo, P., Lehtinen, R., Baxter, S., Toto, T., and Johnson, K. L.: Comparison of Vaisala radiosondes RS41 and RS92 at the ARM Southern Great Plains site, Atmos. Meas. Tech., 9, 3115–3129, https://doi.org/doi:10.5194/amt-9-3115-2016, 2016.

Katzwinkel, J., Siebert, H., and Shaw, R. A.: Observation of a Self-Limiting, Shear-Induced Turbulent Inversion Layer Above Marine Stratocumulus, Bound.-Lay. Meteorol., 145, 131–143, https://doi.org/10.1007/s10546-011-9683-4, 2012.

Knudsen, E. M., Heinold, B., Dahlke, S., Bozem, H., Crewell, S., Gorodetskaya, I. V., Heygster, G., Kunkel, D., Maturilli, M., Mech, M., Viceto, C., Rinke, A., Schmithüsen, H., Ehrlich, A., Macke, A., Lüpkes, C., and Wendisch, M.: Meteorological conditions during the ACLOUD/PASCAL field campaign near Svalbard in early summer 2017, Atmos. Chem. Phys., 18, 17 995–18 022, https://doi.org/10.5194/acp-18-17995-2018, 2018.

Knust, R.: Polar research and supply vessel POLARSTERN operated by the Alfred-Wegener-Institute., J. Large-Scale Res. Facil., 3, https://doi.org/https://doi.org/10.17815/jlsrf-3-163, 2017.

Lenschow, D. H., Li, X. S., Zhu, C. J., and Stankov, B. B.: The stably stratified boundary layer over the great plains: I. Mean and Turbulence Structure, Bound.-Lay. Meteorol., 42, 95–121, https://doi.org/https://doi.org/10.1007/BF00119877, 1988.

Lenschow, D. H., Mann, J., and Kristensen, L.: How Long Is Long Enough When Measuring Fluxes and Other Turbulence Statistics?, J. Atmos. Ocean. Tech., 11, 661–673, https://doi.org/10.1175/1520-0426(1994)011<0661:HLILEW>2.0.CO;2, https://doi.org/10.1175/1520-0426(1994)011<0661:HLILEW>2.0.CO;2, 1994.

Li, D.: Turbulent Prandtl number in the atmospheric boundary layer - where are we now?, Atmos. Res., 216, 86 – 105, https://doi.org/doi.org/10.1016/j.atmosres.2018.09.015, 2019.

Lilly, D. K.: Models of cloud-topped mixed layers under a strong inversion, Q. J. Roy. Meteor. Soc., 94, 292–309, https://doi.org/10.1002/qj.49709440106, 1968.

Lumley, J. L. and Panofsky, H. A.: The structure of atmospheric turbulence, Interscience Monographs and Texts in Physics and Astronomy, New York: Wiley, 1964.

Macke, A. and Flores, H.: The expeditions PS106/1 and 2 of the research vessel POLARSTERN to the Arctic ocean in 2017, Reports on polar and marine research, Bremerhaven, Alfred Wegener Institute for Polar and Marine Research, 719, https://doi.org/10.2312/BzPM_0719_2018, 2018.

Maslanik, J. and Stroeve, J.: Near-Real-Time DMSP SSMIS Daily Polar Gridded Sea Ice Concentrations, Version 1. nt_20170606_f18_nrt_n., https://doi.org/https://doi.org/10.5067/U8C09DWVX9LM, 1999.

Miloshevich, L. M., Paukkunen, A., Vömel, H., and Oltmans, S. J.: Development and Validation of a Time-Lag Correction for Vaisala Radiosonde Humidity Measurements, J. Atmos. Ocean. Tech., 21, 1305–1327, https://doi.org/10.1175/1520-0426(2004)021<1305:DAVOAT>2.0.CO;2, 2004.

Miloshevich, L. M., Vömel, H., Whiteman, D. N., and Leblanc, T.: Accuracy assessment and correction of Vaisala RS92 radiosonde water vapor measurements, J. Geophys. Res.-Atmos., 114, https://doi.org/10.1029/2008JD011565, 2009.

Morrison, H., de Boer, G., Feingold, G., Harrington, J., Shupe, M. D., and Sulia, K.: Resilience of persistent Arctic mixed-phase clouds, Nat. Geosci., 5, 11–17, https://doi.org/10.1038/ngeo1332, 2012.

Naakka, T., Nygård, T., and Vihma, T.: Arctic Humidity Inversions: Climatology and Processes, J. Climate, 31, 3765 – 3787, https://doi.org/DOI: 10.1175/JCLI-D-17-0497.1, 2018.

Neggers, R. A. J., Chylik, J., Egerer, U., Griesche, H., Schemann, V., Seifert, P., Siebert, H., and Macke, A.: Local and remote controls on Arctic mixed-layer evolution, J. Adv. Model. Earth Sy., 0, https://doi.org/10.1029/2019MS001671, 2019.

Nicholls, S.: The dynamics of stratocumulus: Aircraft observations and comparisons with a mixed layer model, Q. J. Roy. Meteor. Soc., 110, 783–820, https://doi.org/10.1002/qj.49711046603, 1984.

Nicholls, S. and Leighton, J.: An observational study of the structure of stratiform cloud sheets: Part I. Structure, Q. J. Roy. Meteor. Soc., 112, 431–460, https://doi.org/10.1002/qj.49711247209, 1986.

Pleavin, T. D.: Large eddy simulations of Arctic stratus clouds, Ph.D. thesis, University of Leeds, http://etheses.whiterose.ac.uk/4934/, 2013.

Schmithüsen, H.: Upper air soundings during POLARSTERN cruise PS106.1 (ARK-XXXI/1.1), https://doi.org/10.1594/PANGAEA.882736, 2017.

Schmithüsen, H.: Continuous meteorological surface measurement during POLARSTERN cruise PS106/1 (ARK-XXXI/1.1), https://doi.org/10.1594/PANGAEA.886302, 2018.

Sedlar, J. and Shupe, M. D.: Characteristic nature of vertical motions observed in Arctic mixed-phase stratocumulus, Atmos. Chem. Phys, 14, 3461–3478, https://doi.org/10.5194/acp-14-3461-2014, 2014.

Sedlar, J. and Tjernström, M.: Stratiform Cloud—Inversion Characterization During the Arctic Melt Season, Bound.-Lay. Meteorol., 132, 455–474, https://doi.org/10.1007/s10546-009-9407-1, 2009.

Sedlar, J., Shupe, M. D., Tjernström, M., Sedlar, J., Shupe, M. D., and Tjernström, M.: On the Relationship between Thermodynamic Structure and Cloud Top, and Its Climate Significance in the Arctic, J. Climate, 25, 2374–2393, https://doi.org/10.1175/JCLI-D-11-00186.1, 2012.

Seifert, A. and Beheng, K. D.: A two-moment cloud microphysics parameterization for mixed-phase clouds. Part 1: Model description, Meteor. Atmos. Phys., 92, 45–66, https://doi.org/10.1007/s00703-005-0112-4, 2006.

Shupe, M. D., Persson, P. O. G., Brooks, I. M., Tjernström, M., Sedlar, J., Mauritsen, T., Sjogren, S., and Leck, C.: Cloud and boundary layer interactions over the Arctic sea ice in late summer, Atmos. Chem. Phys., 13, 9379–9399, https://doi.org/10.5194/acp-13-9379-2013, 2013.

Smit, H., Kivi, R., Vömel, H., and Paukkunen, A.: Thin Film Capacitive Sensors, In: Kämpfer N. (eds) Monitoring Atmospheric Water Vapour, vol. 10 of *ISSI Scientific Report Series*, Springer, New York, NY, https://doi.org/10.1007/978-1-4614-3909-7_2, 2013.

Solomon, A., Shupe, M. D., Persson, O., Morrison, H., Yamaguchi, T., Caldwell, P. M., and Boer, G. D.: The Sensitivity of Springtime Arctic Mixed-Phase Stratocumulus Clouds to Surface-Layer and Cloud-Top Inversion-Layer Moisture Sources, J. Atmos. Sci., 71, 574 – 595, https://doi.org/DOI: 10.1175/JAS-D-13-0179.1, 2014.

Sotiropoulou, G., Sedlar, J., Forbes, R., and Tjernström, M.: Summer Arctic clouds in the ECMWF forecast model: an evaluation of cloud parametrization schemes, Q. J. Roy. Meteor. Soc., 142, 387–400, https://doi.org/10.1002/qj.2658, 2016.

Sotiropoulou, G., Tjernström, M., Savre, J., Ekman, A. M. L., Hartung, K., and Sedlar, J.: Large-eddy simulation of a warm-air advection episode in the summer Arctic, Q. J. Roy. Meteor. Soc., 144, 2449–2462, https://doi.org/10.1002/qj.3316, 2018.

Stein, A., Draxler, R., Rolph, G., Stunder, B., Cohen, M., and Ngan, F.: NOAA's HYSPLIT atmospheric transport and dispersion modeling system, Bull. Amer. Meteor. Soc., 96, 2059–2077, https://doi.org/http://dx.doi.org/10.1175/BAMS-D-14-00110.1, 2015.

Stevens, B., Ackerman, A. S., Albrecht, B. A., Brown, A. R., Chlond, A., Cuxart, J., Duynkerke, P. G., Lewellen, D. C., Macvean, M. K., Neggers, R. A. J., Sánchez, E., Siebesma, A. P., and Stevens, D. E.: Simulations of Trade Wind Cumuli under a Strong Inversion, J. Atmos. Sci., 58, 1870–1891, https://doi.org/10.1175/1520-0469(2001)058<1870:SOTWCU>2.0.CO;2, 2001.

Stull, R. B.: An introduction to boundary layer meteorology., Kluwer Academic Publishers, Dordrecht, The Netherlands, 1988.

Sun, B., Reale, A., Schroeder, S., Seidel, D. J., and Ballish, B.: Toward improved corrections for radiation-induced biases in radiosonde temperature observations, J. Geophys. Res.-Atmos., 118, 4231–4243, https://doi.org/10.1002/jgrd.50369, 2013.

Tjernström, M., Leck, C., Birch, C. E., Bottenheim, J. W., Brooks, B. J., Brooks, I. M., Bäcklin, L., Chang, R. Y.-W., de Leeuw, G., Di Liberto, L., de la Rosa, S., Granath, E., Graus, M., Hansel, A., Heintzenberg, J., Held, A., Hind, A., Johnston, P., Knulst, J., Martin, M., Matrai, P. A., Mauritsen, T., Müller, M., Norris, S. J., Orellana, M. V., Orsini, D. A., Paatero, J., Persson, P. O. G., Gao, Q., Rauschenberg, C., Ristovski, Z., Sedlar, J., Shupe, M. D., Sierau, B., Sirevaag, A., Sjogren, S., Stetzer, O., Swietlicki, E., Szczodrak, M., Vaattovaara, P., Wahlberg, N., Westberg, M., and Wheeler, C. R.: The Arctic Summer Cloud Ocean Study (ASCOS): overview and experimental design, Atmos. Chem. and Phys., 14, 2823–2869, https://doi.org/10.5194/acp-14-2823-2014, 2014.

Tjernström, M.: Turbulence Length Scales in Stably Stratified Free Shear Flow Analyzed from Slant Aircraft Profiles, J. Appl. Meteorol., 32, 948–963, https://doi.org/10.1175/1520-0450(1993)032<0948:TLSISS>2.0.CO;2, 1993.

Tjernström, M., Shupe, M. D., Brooks, I. M., Achtert, P., Prytherch, J., and Sedlar, J.: Arctic Summer Airmass Transformation, Surface Inversions, and the Surface Energy Budget, J. Climate, 32, 769–789, https://doi.org/10.1175/JCLI-D-18-0216.1, 2019.

Uttal, T., Curry, J. A., McPhee, M. G., Perovich, D. K., Moritz, R. E., Maslanik, J. A., Guest, P. S., Stern, H. L., Moore, J. A., Turenne, R., Heiberg, A., Serreze, M. C., Wylie, D. P., Persson, O. G., Paulson, C. A., Halle, C., Morison, J. H., Wheeler, P. A., Makshtas, A., Welch, H., Shupe, M. D., Intrieri, J. M., Stamnes, K., Lindsey, R. W., Pinkel, R., Pegau, W. S., Stanton, T. P., and Grenfeld, T. C.: Surface Heat Budget of the Arctic Ocean, B. Am. Meteorol. Soc., 83, 255–276, https://doi.org/10.1175/1520-0477(2002)083<0255:SHBOTA>2.3.CO;2, 2002.

Wang, J., Zhang, L., Dai, A., Immler, F., Sommer, M., and Vömel, H.: Radiation Dry Bias Correction of Vaisala RS92 Humidity Data and Its Impacts on Historical Radiosonde Data, J. Atmos. Ocean. Tech., 30, 197–214, https://doi.org/10.1175/JTECH-D-12-00113.1, 2013.

Wendisch, M. and Brenguier, J.-L., eds.: Airborne measurements for environmental research, Wiley-VCH Verlag GmbH & Co. KGaA, Weinheim, Germany, https://doi.org/10.1002/9783527653218, 2013.

Wendisch, M., Macke, A., Ehrlich, A., Lüpkes, C., Mech, M., Chechin, D., Dethloff, K., Velasco, C. B., Bozem, H., Brückner, M., Clemen, H.-C., Crewell, S., Donth, T., Dupuy, R., Ebell, K., Egerer, U., Engelmann, R., Engler, C., Eppers, O., Gehrmann, M., Gong, X., Gottschalk, M., Gourbeyre, C., Griesche, H., Hartmann, J., Hartmann, M., Heinold, B., Herber, A., Herrmann, H., Heygster, G., Hoor, P.,

Jafariserajehlou, S., Jäkel, E., Järvinen, E., Jourdan, O., Kästner, U., Kecorius, S., Knudsen, E. M., Köllner, F., Kretzschmar, J., Lelli, L., Leroy, D., Maturilli, M., Mei, L., Mertes, S., Mioche, G., Neuber, R., Nicolaus, M., Nomokonova, T., Notholt, J., Palm, M., van Pinxteren, M., Quaas, J., Richter, P., Ruiz-Donoso, E., Schäfer, M., Schmieder, K., Schnaiter, M., Schneider, J., Schwarzenböck, A., Seifert, P., Shupe, M. D., Siebert, H., Spreen, G., Stapf, J., Stratmann, F., Vogl, T., Welti, A., Wex, H., Wiedensohler, A., Zanatta, M., and Zeppenfeld, S.: The Arctic Cloud Puzzle: Using ACLOUD/PASCAL Multiplatform Observations to Unravel the Role of Clouds and Aerosol Particles in Arctic Amplification, Bull. Am. Meteor. Soc., 100, 841–871, https://doi.org/10.1175/BAMS-D-18-0072.1, 2019.

Wood, R.: Stratocumulus Clouds, Mon. Weather Rev., 140, 2373–2423, https://doi.org/10.1175/MWR-D-11-00121.1, 2012.

Wyngaard, J. C.: Turbulence in the Atmosphere, Cambridge University Press, 408 p., 2010.